

Research paper

Soil-water strong coupled ISPH based on $\mathbf{u} - \mathbf{w} - p$ formulation for large deformation problems

Daniel S. Morikawa*, Mitsuteru Asai

Kyushu University, 744 Motooka Nishi-ku, Fukuoka, Japan



ARTICLE INFO

MSC:

00-01
99-00

Keywords:

SPH method
ISPH
Saturated soil
Slope stability
Incompressible pore fluid

ABSTRACT

This paper is dedicated to the introduction of a strong coupled soil–water interaction formulation based on an incompressible smoothed particle hydrodynamics (ISPH) framework. The method is based on the \mathbf{u} – \mathbf{w} – p Biot's formulation and adapted to a semi-implicit projection method for incompressibility condition of pore water and soil grains. The SPH Lagrangian particles move according to the soil velocity, while water variables are embedded into such soil particles. This allows to solve the pressure Poisson equation in a strong coupling way, in addition to enable to update the Darcy's drag force implicitly. A simple boundary treatment on natural boundary conditions for soil particle is proposed to take into account both non-penetration and friction effects. The proposed method was verified and validated through a series of numerical tests resulting in good agreements with both theoretical and experimental results. Finally, we show the applicability of the proposed method in the famous Selborne experiment, a full-scale slope failure problem.

1. Introduction

The smoothed particle hydrodynamics (SPH) method is a Lagrangian mesh-less numerical method developed by Gingold and Monaghan (1977) and Lucy (1977). The greatest advantage of SPH over mesh-based methods such as the finite element method (FEM) is the free moving nature of its Lagrangian particles. Hence, the SPH does not suffer from usual difficulties caused by mesh distortion in highly dynamic problems.

The current work is based on SPH's incompressible form (ISPH), which was first developed by Cummins and Rudman (1999) and later applied and enhanced in many forms (Pozorski and Wawrzenczuk, 2002; Khayyer et al., 2008; Asai et al., 2012; Barcarolo et al., 2014; Morikawa et al., 2019, 2021; Morikawa and Asai, 2021; Asai et al., 2021). Its main feature is to impose incompressibility from a projection method similar to the moving-particle semi-implicit method (MPS) (Koshizuka and Oka, 1996), which results in a pressure Poisson equation (PPE).

Application of SPH to Geomechanics problems can probably be dated back to 2004 with Maeda et al. (2004)'s work (later translated to English in Maeda et al. (2006)). However, due to language barriers, this paper was restricted to the Japanese research scene. Internationally, one of the earlier works of SPH to Geomechanics problems can be credited to Naili et al. (2005), who have used SPH with a non-Newtonian rheology model to simulate liquefaction. Due to the Lagrangian nature of SPH particles and its wide use in Fluid Mechanics, most applications of SPH to Geomechanics have focused on approximating the 'colloidal'

soil as a fluid-like material. With this same approach, Cascini et al. (2014) utilized SPH for channelized landslides, and Lin et al. (2019) coupled partitioned finite elements and interface elements method to predict whether a previously defined slip surface would fail with SPH to simulate the landslide flow as a fluid-like material.

One problem of this approach is that it does not interact with the great achievements of Geomechanics material modeling, such as the concept of consolidation and drained/undrained behavior to predict the initiation of colloidal state for Geomaterials. Instead, it focuses on very specific behavior of soils under specific conditions. Hence, it is impossible to verify and validate such formulations with typical Soil Mechanics benchmark tests.

Early attempts to derive purely Geomechanics formulations on SPH can be retrieved from Bui et al. (2008), where they focus on the behavior of dry soil using elastoplastic material based on Drucker–Prager constitutive model. It was followed by Bui and Fukagawa (2009), where they conducted a first attempt of the soil–water coupled problem with the \mathbf{u} – p formulation under the assumption of two phases—one point framework. Later, Bui and Nguyen (2017) coupled the previously mentioned dry soil SPH formulation with water SPH particles, which can be called a two points–two phases framework.

From our point of view, although Bui and Nguyen (2017)'s method was a notable advance in the topic of application of SPH to Geomechanics, we believe that this work has some important shortcomings. First,

* Corresponding author.

E-mail address: daniel@civil.doc.kyushu-u.ac.jp (D.S. Morikawa).

the behavior of pressure dissipation over time has not been assessed by this method. Although it surely contains the necessary equations to simulate it, the authors chose to not include any numerical test that addresses this topic, which is an essential feature of Soil Mechanics. In addition, the integration of permeability (the drag force) is necessarily explicit, since the water and soil particles are separated, which makes a large constraint on its value range in relation to time increment (as explained in Section 3 and demonstrated in Section 8.2).

Similarly to Bui and Fukagawa (2009), Blanc and Pastor (2012) developed a coupled SPH method for the $\mathbf{u}-p$ formulation (Zienkiewicz et al., 1999), in which it is assumed that the pore water undergoes as static seepage, that is, the acceleration of water in relation to the soil skeleton is neglected. Since then, there were some developments on this method, mainly coupling it with fluid-like rheology models (Pastor et al., 2015).

Although not under the scope of this work, because it does not consider the movement of the soil itself, it is important to cite the great work of Lian et al. (2021) for having developed a SPH framework for dealing with the seepage flow through unsaturated soil. We recommend the recent paper from Bui and Bguyen (2021) for readers interested in reviewing the state-of-art of SPH for Geomechanics problems.

However, there is a vacuum of studies using SPH with the full $\mathbf{u}-\mathbf{w}-p$ formulation (Biot, 1956), which might be important to problems that involve high-frequency loadings such as earthquakes and problems with soil of low permeability (Zienkiewicz et al., 1999), since the relative acceleration of pore water with respect to the soil skeleton is an important factor.

In this work, we propose a strong coupling ISPH based on the $\mathbf{u}-\mathbf{w}-p$ Biot's formulation (Biot, 1956) to expand application to dynamic seepage flow problems with low permeability. The incompressibility is then applied to enforce both pore fluid and soil grains as incompressible, which results in a strong coupled PPE. A considerable amount of inspiration for this method has been taken from developments on the material point method (MPM) with their great works in this topic such as Kularathna et al. (2021).

The current formulation treats soil skeleton deformation in a Lagrangian manner, while water variables are integrated into the soil particles (called one point–two phases). The soil material is modeled with conventional elastoplastic constitutive laws and a return mapping technique that can be easily adapted to any constitutive model (in this work, we use only Mohr–Coulomb and modified Cam–Clay models). The boundary treatment is heavily simplified due to simple constraints on velocity and pressure, and numerical tests show a good applicability of this boundary condition. Finally, an example using the Selborne experiment (Cooper et al., 1998; Bromhead et al., 1998) is conducted to show the robustness of our proposed method.

2. Coupling porous media–water formulation

This section is devoted to define the essential variables for the Geomechanics analysis and its governing equations. We follow the so-called Biot formulation (Biot, 1956) (also called $\mathbf{u}-\mathbf{w}-p$ formulation) in a similar manner as explained in Zienkiewicz et al. (1999). The main difference is the constraint that both soil grains and pore water are treated as incompressible in this study. Hence, all parameters related to compressibility of grains and water are disregarded. Also, we are using soil skeleton velocity \mathbf{v} instead of displacement \mathbf{u} and water velocity \mathbf{v}_w instead of Darcy's velocity \mathbf{w} to better adapt into the SPH framework.

2.1. Background definitions

Here, we define the standard nomenclature and symbols of common terms in Geomechanics used throughout the article. First, consider a control volume of saturated soil as in Fig. 1. The average velocity of soil grains are represented as \mathbf{v} , while the average velocity of pore water as \mathbf{v}_w . Notice that the actual movement of the Lagrangian SPH

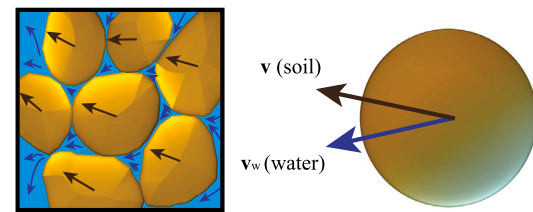


Fig. 1. Schematic illustration of the soil skeleton velocity \mathbf{v} and water velocity \mathbf{v}_w .

particles are updated according to the soil skeleton velocity, while the pore water velocity is treated as an internal variable of the particle. Hence, we use the material time derivative of \mathbf{v} and the local time derivative of \mathbf{v}_w .

The material and local derivatives are defined as, respectively,

$$\frac{D(\cdot)}{Dt} = \frac{\partial(\cdot)}{\partial t}, \quad (1)$$

$$\frac{D(\cdot)}{Dt} = \frac{\partial(\cdot)}{\partial t} + (\mathbf{v} \cdot \nabla)(\cdot), \quad (2)$$

where t represents time.

We also define a third velocity-like parameter called Darcy's velocity \mathbf{w} , which is defined as the average water discharge over a unit cross section area (units of $[\text{length}]^3/([\text{time}][\text{length}]^2)$, in other words, volume per time per area). The relationship between \mathbf{v} , \mathbf{v}_w and \mathbf{w} for saturated soils can be written as

$$\mathbf{w} = n(\mathbf{v}_w - \mathbf{v}), \quad (3)$$

where n is the porosity.

Given the density of soil grains ρ_s and the water density ρ_w , the mixture density is defined as

$$\rho = (1 - n)\rho_s + n\rho_w. \quad (4)$$

Finally, as common practice in Geotechnical Engineering, we split the Cauchy stress tensor σ into the effective stress σ' and pore water pressure p as (Zienkiewicz et al., 1999)

$$\sigma = \sigma' - \alpha p \mathbf{I}, \quad (5)$$

where \mathbf{I} is the identity matrix and $\alpha = 1 - K_T/K_s$ is a scalar related to the ratio of soil skeleton bulk modulus K_T to solid grains bulk modulus K_s . Notice that we use the traction positive sign convention for stress.

2.2. Original governing equations

The original set of governing equations are: linear momentum equilibrium of the mixture, linear momentum equilibrium of the internal pore water and the conservation of mass for the water part. For readers interested in the derivation of such equations, please refer to Zienkiewicz et al. (1999).

- Mixture linear momentum equilibrium

$$\rho \frac{D\mathbf{v}}{Dt} = \nabla \cdot \sigma + \rho g - \rho_w \frac{D\mathbf{w}}{Dt}. \quad (6)$$

- Pore water linear momentum equilibrium

$$\rho_w \frac{D\mathbf{v}_w}{Dt} = \nabla p + \rho_w \mathbf{g} - \frac{\rho_w}{n} \frac{D\mathbf{w}}{Dt} - \mathbf{R}. \quad (7)$$

- Pore water mass conservation

$$\nabla \cdot \mathbf{w} + \alpha \nabla \cdot \mathbf{v} + \frac{1}{Q} \frac{\partial p}{\partial t} + \frac{n}{\rho_w} \dot{\rho}_w + \dot{s} = 0. \quad (8)$$

In the above equations, \mathbf{g} is the gravity acceleration vector, \mathbf{R} is the Darcy's drag force, $1/Q = n/K_w + (\alpha - n)/K_s$ is a parameter related to the mixture compressibility (K_w is the water bulk modulus) and \dot{s} is the rate of soil grains volume expansion due to external conditions such as temperature change.

\mathbf{R} is defined as $\mathbf{R} = \rho_w g \mathbf{k}^{-1} \mathbf{w}$, where g is the gravity acceleration norm and \mathbf{k} is the permeability tensor which takes into account anisotropic permeability. In this study, we consider the isotropic case; hence, \mathbf{k} is simplified as a scalar k , and \mathbf{R} becomes

$$\mathbf{R} = \frac{\rho_w g}{k} \mathbf{w}, \quad (9)$$

with \mathbf{k} dimensions being [length]/[time].

An additional equation must be defined for the mass conservation of the solid skeleton in order to update the porosity n . Similarly to [Bandara and Soga \(2015\)](#) and [Bui and Nguyen \(2017\)](#), we define this equation in terms of the soil skeleton density $(1-n)\rho_s$ and its velocity \mathbf{v} ,

$$\frac{D[(1-n)\rho_s]}{Dt} + \nabla \cdot [(1-n)\rho_s \mathbf{v}] = 0. \quad (10)$$

2.3. Governing equations in the incompressibility limit

In the incompressibility limit, most of the equations explained until now can be simplified, while maintaining Mathematical precision. Basically, K_s and K_w are regarded as infinite, while the time derivative of density is null. In addition, we are not considering any thermal expansion in this study. As a consequence,

$$\alpha = 1, \quad \frac{1}{Q} = \dot{\rho}_w = \dot{s} = 0 \quad (11)$$

The linear momentum equilibrium equation for the mixture (Eq. (6)) written as a function of effective stress (Eq. (5)) for incompressible soil particle (Eq. (11)) becomes

$$\frac{D\mathbf{v}}{Dt} = \nabla \cdot \boldsymbol{\sigma}' - \nabla p + \rho \mathbf{g} - \rho_w \frac{D\mathbf{w}}{Dt}, \quad (12)$$

while the linear momentum for the water phase (Eq. (7)) does not change within the incompressibility limit.

Using Eq. (11) on Eq. (8), mass conservation for the water phase becomes

$$\nabla \cdot \mathbf{w} + \nabla \cdot \mathbf{v} = 0. \quad (13)$$

Exchanging \mathbf{w} to \mathbf{v}_w through Eq. (3), we derive

$$n \nabla \cdot \mathbf{v}_w + (1-n) \nabla \cdot \mathbf{v} = 0. \quad (14)$$

Similarly, Eq. (10) might be simplified disregarding the time and spatial derivative of ρ_s , hence

$$\frac{Dn}{Dt} = \nabla \cdot [(1-n)\mathbf{v}]. \quad (15)$$

Remark 1. The incompressibility limit does not mean that the whole soil skeleton is incompressible. Instead, it only means that pore water and soil grains are incompressible. Soil skeleton compressibility depends on the constitutive model chosen and its parameters. The variable controlling numerical density of the SPH particle is the porosity, which is updated using Eq. (15).

Remark 2. In theory, to consider true compressibility of pore water and/or soil grains, it would be necessary additional equations to account for the change in density, since we already have four equations (Eqs. (6), (7), (8) and (10)) and four unknowns (\mathbf{v} , \mathbf{v}_w , n , p). Some studies such as the book in which we based our formulation ([Zienkiewicz et al., 1999](#)), as well as [Blanc and Pastor \(2012\)](#) and [Bandara and Soga \(2015\)](#), have considered an incomplete incompressibility constraint, i.e., considering the time derivative of densities as zero while maintaining the term $1/Q$. In such case, the term $1/Q$ works similarly to a damping parameter to the pressure estimation. However, this approach slightly reduces Mathematical precision and consistency.

3. Projection method

Here, we explain the projection method used in the present work. The basic idea is to project the velocity into an explicit predictor step, where pressure is not taken into account, and then correct this velocity with the influence of pressure implicitly. Hence, its description as a semi-implicit method. All time derivatives are evaluated with first order symplectic operators, i.e.,

$$\frac{\partial(\cdot)}{\partial t} = \frac{(\cdot)^{\beta+1} - (\cdot)^\beta}{\Delta t}, \quad (16)$$

where Δt is the time increment, and the superscripts β and $\beta + 1$ represent the current and next time steps, respectively.

Before starting, it is necessary to derive the linear momentum equilibrium equations in terms of \mathbf{v}_w and isolating water from soil acceleration terms and vice-versa. Multiplying Eq. (12) by $1/n$ and subtracting by Eq. (7), we can eliminate the Darcy's acceleration term ($D\mathbf{w}/Dt$). Including Eqs. (3), (9) and the definition of the mixture density (Eq. (4)), after some algebra, we finally derive the linear momentum conservation for the soil skeleton as

$$\frac{D\mathbf{v}}{Dt} = \mathbf{g} + \frac{1}{(1-n)\rho_s} \nabla \cdot \boldsymbol{\sigma}' - \frac{1}{\rho_s} \nabla p + \frac{n^2 \rho_w g}{(1-n)\rho_s k} (\mathbf{v}_w - \mathbf{v}). \quad (17)$$

Similarly, we derive the final form for the water conservation of linear momentum applying Eqs. (3), (9) on Eq. (7), and remembering that \mathbf{v}_w is updated with the local derivative (Eq. (2)),

$$\frac{\partial \mathbf{v}_w}{\partial t} = \mathbf{g} - (\mathbf{v} \cdot \nabla) \mathbf{v}_w - \frac{1}{\rho_w} \nabla p - \frac{n^2 \rho_w g}{n \rho_w k} (\mathbf{v}_w - \mathbf{v}). \quad (18)$$

The drag force on Eq. (18) can be obviously further simplified, but we are showing in this form to highlight the symmetry between soil to water and water to soil forces. Classically, the drag force term is placed in the predictor step as an explicit force, so that the predictor step becomes

$$\begin{cases} \mathbf{v}^* = \mathbf{v}^\beta + \Delta t \left(\mathbf{g} + \frac{1}{(1-n)\rho_s} \nabla \cdot \boldsymbol{\sigma}'^\beta + \frac{n^2 \rho_w g}{(1-n)\rho_s k} (\mathbf{v}_w^\beta - \mathbf{v}^\beta) \right) \\ \mathbf{v}_w^* = \mathbf{v}_w^\beta + \Delta t \left(\mathbf{g} - (\mathbf{v}^\beta \cdot \nabla) \mathbf{v}_w^\beta - \frac{ng}{k} (\mathbf{v}_w^\beta - \mathbf{v}^\beta) \right), \end{cases} \quad (19)$$

Notice that the drag force is composed by a scalar term multiplied by a relative velocity. Hence, if explicitly integrated in time, such as in [Bui and Nguyen \(2017\)](#), the conditions

$$a = \Delta t \frac{n^2 \rho_w g}{(1-n)\rho_s k} < 1 \quad \& \quad b = \Delta t \frac{ng}{k} < 1 \quad (20)$$

must be verified for the drag force to maintain its stability (see Section 8.2). This would lead to a critical constraint on Δt if k is very small. To solve this problem, some studies such as [Kularathna et al. \(2021\)](#) include the drag force into the predictor step and make it implicit in relation to the predicted velocity, so that

$$\begin{cases} \mathbf{v}^* = \mathbf{v}^\beta + \Delta t \left(\mathbf{g} + \frac{1}{(1-n)\rho_s} \nabla \cdot \boldsymbol{\sigma}'^\beta + \frac{n^2 \rho_w g}{(1-n)\rho_s k} (\mathbf{v}_w^* - \mathbf{v}^*) \right) \\ \mathbf{v}_w^* = \mathbf{v}_w^\beta + \Delta t \left(\mathbf{g} - (\mathbf{v}^\beta \cdot \nabla) \mathbf{v}_w^\beta - \frac{ng}{k} (\mathbf{v}_w^* - \mathbf{v}^*) \right). \end{cases} \quad (21)$$

Although it can relieve the above-mentioned constraint in the time increment, it loses Mathematical consistency since the predicted velocity is not a proper physical quantity. Instead, we suggest to calculate the drag force implicitly and include it into the correction step to maintain its physical meaning.

The predictor step in this proposed method is then defined as

$$\begin{cases} \mathbf{v}^* = \mathbf{v}^\beta + \Delta t \left(\mathbf{g} + \frac{1}{(1-n)\rho_s} \nabla \cdot \boldsymbol{\sigma}'^\beta \right) \\ \mathbf{v}_w^* = \mathbf{v}_w^\beta + \Delta t \left(\mathbf{g} - (\mathbf{v}^\beta \cdot \nabla) \mathbf{v}_w^\beta \right). \end{cases} \quad (22)$$

A comparison between the three methods of drag force time integration above (here called "drag force explicit", "drag force predictor-implicit" and "drag force implicit") is shown in Section 8.2.

Then, corrector step including the implicit drag force term is calculated as

$$\begin{cases} \mathbf{v}^{\beta+1} = \mathbf{v}^* + \Delta t \left(-\frac{1}{\rho_s} \nabla p^{\beta+1} + \frac{n^2 \rho_w g}{(1-n)\rho_s k} (\mathbf{v}_w^{\beta+1} - \mathbf{v}^{\beta+1}) \right) \\ \mathbf{v}_w^{\beta+1} = \mathbf{v}_w^* + \Delta t \left(-\frac{1}{\rho_w} \nabla p^{\beta+1} - \frac{ng}{k} (\mathbf{v}_w^{\beta+1} - \mathbf{v}^{\beta+1}) \right). \end{cases} \quad (23)$$

Isolating the $\beta + 1$ velocity terms of Eqs. (23) to the left-hand side, we have

$$\begin{cases} (1+a)\mathbf{v}^{\beta+1} + (-a)\mathbf{v}_w^{\beta+1} = \mathbf{v}^* - \frac{\Delta t}{\rho_s} \nabla p^{\beta+1} \\ (-b)\mathbf{v}^{\beta+1} + (1+b)\mathbf{v}_w^{\beta+1} = \mathbf{v}_w^* - \frac{\Delta t}{\rho_w} \nabla p^{\beta+1}, \end{cases} \quad (24)$$

where a and b are defined in Eq. (20).

Solving Eqs. (24) for velocity we derive the final form of the corrector step as

$$\begin{cases} \mathbf{v}^{\beta+1} = \frac{1}{1+a+b} \left((1+b)\mathbf{v}^* + a\mathbf{v}_w^* - \Delta t \left(\frac{1+b}{\rho_s} + \frac{a}{\rho_w} \right) \nabla p^{\beta+1} \right) \\ \mathbf{v}_w^{\beta+1} = \frac{1}{1+a+b} \left(b\mathbf{v}^* + (1+a)\mathbf{v}_w^* - \Delta t \left(\frac{b}{\rho_s} + \frac{1+a}{\rho_w} \right) \nabla p^{\beta+1} \right). \end{cases} \quad (25)$$

Next, we developed a pressure Poisson equation (PPE) as follows. First, consider the incompressible conservation of mass for the water phase as in Eq. (14). The above equations of the corrector step (Eqs. (25)) can be applied into Eq. (14) directly, and, after some rearranging, we obtain

$$\nabla^2 p^{\beta+1} = \frac{1-n+b}{C} \nabla \cdot \mathbf{v}^* + \frac{n+a}{C} \nabla \cdot \mathbf{v}_w^*, \quad (26)$$

where

$$C = \Delta t \left(\frac{1-n+b}{\rho_s} + \frac{n+a}{\rho_w} \right), \quad (27)$$

which is an implicit equation that must be calculated through a linear solver. In this study, we have chosen the conjugate gradient method, since the left hand side of Eq. (26) is positive and symmetric.

Finally, with the pressure profile calculated, we update the velocities with the corrector step (Eq. (25)) and update the position of the particle with a first order symplectic time integration scheme (Eq. (16)) as

$$\mathbf{x}^{\beta+1} = \mathbf{x}^\beta + \Delta t \mathbf{v}^{\beta+1}. \quad (28)$$

4. Effective stress update

In this section, we explain the effective stress update and the return mapping technique used in this proposed method. Most previous works such as Bui et al. (2008) derive an elastoplastic tangent moduli for an specific constitutive model. Then, the stress is updated with a single equation that incorporates both elastic and plastic parts.

In this work, however, we show a more generalized form of the return mapping called elastic predictor/plastic corrector algorithm, as explained in de Souza Neto et al. (2008). Here, the stress update is divided into two steps: an elastic predictor step (leading to a trial state σ'^{trial}) and a plastic corrector step (return mapping leading to $\sigma'^{\beta+1}$). A schematic illustration of this method is shown in Fig. 2. In comparison, the elastoplastic tangent moduli would be a straight line from σ'^β to $\sigma'^{\beta+1}$ in Fig. 2.

The reason for choosing a more general technique is to make it easier to adapt to any plastic constitutive model as pleased. Also, this technique is very convenient for complex constitutive models such as the modified Cam–Clay, in which a Newton–Raphson routine guarantees the stability and accuracy of the return mapping taking into account any type of hardening rule (see Appendix B). The objective here is to merely show the implementation of such techniques into the SPH framework, rather than deriving the formulation. Readers interested in more details should refer to de Souza Neto et al. (2008).

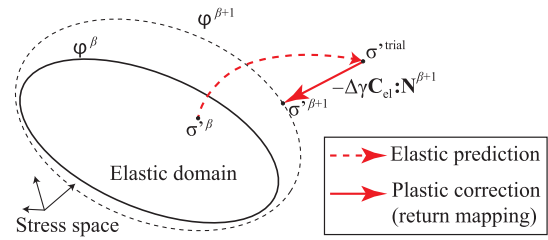


Fig. 2. Schematic illustration of the return mapping.

4.1. Return mapping

Before starting, we must define the yield function φ , the flow rule Ψ and any set of hardening variables α , which depend on the plastic constitutive model chosen. Here, we use either the Mohr–Coulomb or the modified Cam–Clay models depending on the problem.

Then, we define the elastic trial state for the effective stress σ'^{trial} , which depends on the elastic constitutive model. Here, it was chosen the hypoelastic material with the Jaumann rate update.

Then, we check whether the trial state lies within the plastic yield condition $\varphi(\sigma'^{\text{trial}}, \alpha'^{\text{trial}}) \leq 0$. If so, trial state is considered to be correct and the material is under pure elastic deformation. If not, the trial stress is corrected as

$$\sigma'^{\beta+1} = \sigma'^{\text{trial}} - \Delta\gamma \mathbf{C}_{el} : \mathbf{N}^{\beta+1}, \quad (29)$$

where $\Delta\gamma$ is the plastic multiplier (amount of plastic correction) and $\mathbf{N} = \partial\Psi/\partial\sigma'$ is the direction of the plastic flow. The superscript $\beta + 1$ is to represent that the correction is applied in order to accommodate the yield function to this new configuration (i.e., $\varphi^{\beta+1} = \varphi(\sigma'^{\beta+1}, \alpha'^{\beta+1}) = 0$), as in Fig. 2.

4.2. Hypoelasticity

As usual in Soil Mechanics, the constitutive model is only applied to the effective stress, rather than the Cauchy stress. Our proposed method describes the elastic behavior of the soil skeleton as a hypoelastic material using the Jaumann rate for time integration. The Jaumann rate in terms of the effective stress can be expressed as

$$\frac{D\sigma'}{Dt} = \mathbf{C}_{el} : \mathbf{D} + \mathbf{W} \cdot \sigma' + \sigma' \cdot \mathbf{W}^T, \quad (30)$$

$$\mathbf{D} = \frac{1}{2}(\mathbf{L} + \mathbf{L}^T), \quad (31)$$

$$\mathbf{W} = \frac{1}{2}(\mathbf{L} - \mathbf{L}^T), \quad (32)$$

$$\mathbf{L} = (\nabla \otimes \mathbf{v})^T, \quad (33)$$

where T is the transpose operator, \mathbf{D} and \mathbf{W} are the rate-of-deformation and spin tensors related to the spatial gradient of velocity \mathbf{L} , and \mathbf{C}_{el} is the Hookean elastic material tangent moduli.

Integrating Eq. (30) explicitly, we have

$$\sigma'^{\beta+1} = \sigma'^\beta + \Delta t (\mathbf{C}_{el} : \mathbf{D}^{\beta+1} + \mathbf{W}^{\beta+1} \cdot \sigma'^\beta + \sigma'^\beta \cdot (\mathbf{W}^{\beta+1})^T). \quad (34)$$

The superscript $\beta + 1$ for \mathbf{D} and \mathbf{W} in Eq. (34) are due to the fact that the stress is updated after the velocity (i.e., $\mathbf{L}^{\beta+1} = (\nabla \otimes \mathbf{v}^{\beta+1})^T$).

This elastic stress update might be used exactly in this form as in Section 8.2 when the soil skeleton is considered to be purely elastic. Alternatively, it is regarded as the trial state of the return mapping algorithm in case of an elastoplastic material, i.e.,

$$\sigma'^{\text{trial}} = \sigma'^\beta + \Delta t (\mathbf{C}_{el} : \mathbf{D}^{\beta+1} + \mathbf{W}^{\beta+1} \cdot \sigma'^\beta + \sigma'^\beta \cdot (\mathbf{W}^{\beta+1})^T). \quad (35)$$

For a detailed explanation on the implementation of the return mapping for Mohr–Coulomb and modified Cam–Clay, refer to Appendices A and B, respectively.

5. The SPH method

The SPH method is a numerical scheme in which the domain is discretized into Lagrangian particles in the context of Continuum Mechanics. The general idea is to approximate a function f and its spatial derivatives based on such function values contained in neighboring particles according to a weight parameter W also called kernel. Mathematically, the primordial SPH approximation can be denoted as

$$\langle f \rangle_i = \sum_{j=1}^N \frac{m_j}{\rho_j} f_j W(\mathbf{r}_{ij}, h), \quad (36)$$

where i and j represent a target and a neighbor particle, respectively, m the mass, ρ the density, $\mathbf{r}_{ij} = \mathbf{x}_i - \mathbf{x}_j$ the relative position vector, N the total number of particles and h the smoothing length, which, in this study, has been chosen to be $h = 1.2d$ (d is the particle diameter).

Originally, the first derivative of a function in SPH is calculated as

$$\langle \nabla f \rangle_i = \sum_{j=1}^N \frac{m_j}{\rho_j} (f_j - f_i) \nabla W(\mathbf{r}_{ij}, h), \quad (37)$$

However, as widely known in the SPH community,

$$\langle \nabla f \rangle_i = \frac{1}{\rho_i} \sum_{j=1}^N m_j (f_j - f_i) \nabla W(\mathbf{r}_{ij}, h), \quad (38)$$

and

$$\langle \nabla f \rangle_i = \rho_i \sum_{j=1}^N m_j \left(\frac{f_i}{\rho_i^2} + \frac{f_j}{\rho_j^2} \right) \nabla W(\mathbf{r}_{ij}, h) \quad (39)$$

are usually much more stable than Eq. (37). Notice that Eqs. (38) and (39) are easily derived from Eq. (37) taking the derivative of ρf and f/ρ , respectively (Monaghan, 1992).

Many researchers have attempted to increase the accuracy of the SPH first derivative approximation. As initially developed by Randles and Libersky (1996) and followed by Bonet and Lok (1999), Eq. (38) can be expanded as

$$\langle \nabla f \rangle_i = \frac{1}{\rho_i} \sum_{j=1}^N m_j (f_j - f_i) \tilde{\nabla} W(\mathbf{r}_{ij}, h), \quad (40)$$

where

$$\tilde{\nabla} W(\mathbf{r}_{ij}, h) = \mathbf{B}_i \nabla W(\mathbf{r}_{ij}, h), \quad (41)$$

and

$$\mathbf{B}_i = \left(\frac{1}{\rho_i} \sum_{j=1}^N m_j \nabla W(\mathbf{r}_{ij}, h) \otimes \mathbf{r}_{ji} \right)^{-1}. \quad (42)$$

This formulation has the advantage of being first order consistent, which means that it can solve the gradient of a linear function exactly. As a backside, it is not conservative, meaning that the effect of, say, particle i on particle j is not the same as of particle j on i . Hence, if used in the calculation of a force, it might not conserve linear momentum exactly.

Ganzenmüller (2015) developed another formulation on the first derivative based on Eq. (39) expressed as

$$\langle \nabla f \rangle_i = \rho_i \sum_{j=1}^N m_j \left(\frac{f_i}{\rho_i^2} \tilde{\nabla} W(\mathbf{r}_{ij}, h) - \frac{f_j}{\rho_j^2} \tilde{\nabla} W(\mathbf{r}_{ji}, h) \right), \quad (43)$$

which is conservative, but loses its first order consistency. To visualize the conservative property of Eq. (43), we can rewrite it as

$$\langle \nabla f \rangle_i = \rho_i \sum_{j=1}^N m_j \left(\mathbf{B}_i \frac{f_i}{\rho_i^2} + \mathbf{B}_j \frac{f_j}{\rho_j^2} \right) \nabla W(\mathbf{r}_{ij}, h). \quad (44)$$

As clearly seen in Eq. (44), the force exerted from particles i to j is the same as its counterpart from j to i .

The usage of Eqs. (40) and (43) as opposed to (38) and (39) is very important in the context of elasticity, since Eqs. (38) and (39) are not capable of preserving angular momentum, as explained by Bonet and Lok (1999) and Lee et al. (2016). Because of its first order consistency, Eq. (40) is preferred over Eq. (43), except when applied to the stress tensor, where being conservative is crucial to the overall accuracy.

Finally, the Laplacian of a function might be estimated as

$$\langle \nabla^2 f \rangle_i = \frac{2}{\rho_i} \sum_{j=1}^N m_j \frac{\mathbf{r}_{ij} \cdot \nabla W(\mathbf{r}_{ij}, h)}{\mathbf{r}_{ij}^2} (f_i - f_j), \quad (45)$$

which is a combination of SPH and finite difference methods proposed by Morris et al. (1997). Although there are some attempts to improve the accuracy of SPH second derivatives such as Faheti and Manzari (2011), we decided to maintain using Eq. (45), since it already provide reasonable solutions for our numerical examples.

In these equations, $\nabla = (\frac{\partial}{\partial x}, \frac{\partial}{\partial y}, \frac{\partial}{\partial z})$ is the nabla operator and $\langle \rangle$ represent the SPH approximation. For all numerical analysis in this study, we have chosen the cubic spline (Schoenberg, 1964) for the kernel W .

6. Application of SPH approximations on governing equations

Up to now, all equations were written in a generic form that could be applied to any numerical method. Here, we include some additional attributes of the proposed method such as stabilization procedures and boundary conditions. In addition, we clearly show how to implement SPH approximations from Section 5 into the results of Sections 2–4.

6.1. Stabilization

Similarly to previous works such as Lee et al. (2016) and Morikawa and Asai (2021), we include the JST stabilization term to avoid numerical instabilities in our elastoplastic model based on the Hypoelasticity. Since this procedure has already been well documented in both references above, we abstain from longer explanations in this study.

Including the stabilization parameter C_{JST} in the predictor step of the linear momentum equation for the soil phase, it becomes

$$\mathbf{v}^* = \mathbf{v}^\beta + \Delta t \left(\mathbf{g} + \frac{1}{(1-n)\rho_s} \nabla \cdot \boldsymbol{\sigma}'^\beta + \mathbf{C}_{JST}^\beta \right), \quad (46)$$

where

$$\mathbf{C}_{JST} = c_p d(\epsilon^{(2)} \nabla_0^2 \mathbf{v}), \quad (47)$$

c_p is the p-wave velocity defined as

$$c_p = \sqrt{\frac{K + \mu/3}{(1-n)\rho_s}}, \quad (48)$$

and $\epsilon^{(2)}$ is a chosen coefficient.

Differently than Lee et al. (2016) and Morikawa and Asai (2021), we do not include a fourth order term, since we concluded that it is not necessary for our purposes. In our numerical tests, this parameter was sufficient to stabilize the whole formulation for a large number of time iterations. No stabilization in the water phase were necessary. In general, we chose higher values of $\epsilon^{(2)}$ (as large as 0.5) for particles with elastic deformation, while we found to be important to maintain very small values (usually 0.01) when the particle is under plastic deformation to avoid unphysical damping behavior.

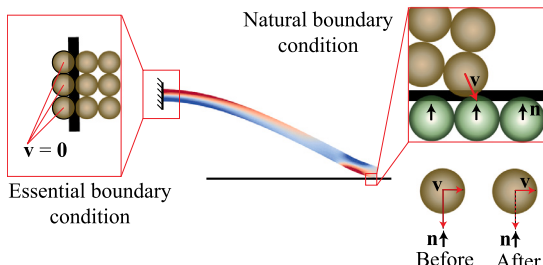


Fig. 3. Schematic illustration of essential (left) and natural (right) boundary conditions.

6.2. Boundary conditions

In this formulation, essential boundary conditions are trivially attributed simply assigning a specific value of a designated variable to the particles in the boundary domain. For the natural boundary condition, we introduce a simplified wall boundary condition which takes into account both non-penetration and friction effects.

A graphical representation of essential and natural boundary conditions is shown in Fig. 3 exemplified as a cantilever beam fixed at the left end and being supported by the floor at the right end. In this example, the particles inside the left wall are assigned with zero velocity while the particles hitting the floor have their velocities in the normal direction \mathbf{n} erased (dashed velocity vector) as part of the non-penetration condition. This approach is the same as the one promoted in Morikawa and Asai (2021).

Other instances of essential boundary conditions are zero pressure at free-surfaces and zero water velocity at an impermeable wall boundary. In this work, we define a particle at the free-surface if there are less than a certain number of neighboring particles (for cubic spline kernel, 48 in 3-D simulations).

Let us explain in more details the natural boundary conditions. First, a layer of wall particles is defined throughout the wall domain, each particle with a pre-defined normal direction pointing to the wall surface. Then, once the physical soil particle approaches the wall, its velocity is numerically set to zero at the wall normal direction.

In mathematical terms, let us call \mathbf{v}' the relative velocity between soil particle and wall particle ($\mathbf{v}' = \mathbf{v} - \mathbf{v}_{\text{wall}}$) before non-penetration correction and \mathbf{v}'' the corrected velocity. Then,

$$\mathbf{v}'' = \mathbf{v}' - (\mathbf{n} \cdot \mathbf{v}')\mathbf{n}. \quad (49)$$

In this study, we also include the effect of wall friction on the natural boundary condition. First, notice that the term $-(\mathbf{n} \cdot \mathbf{v}')\mathbf{n}$ from Eq. (49) can be interpreted as an acceleration \mathbf{a}_n due to the applied force from the wall, as

$$\mathbf{a}_n = -\frac{(\mathbf{n} \cdot \mathbf{v}')}{\Delta t}\mathbf{n}. \quad (50)$$

The amplitude of the friction force \mathbf{f}_{fric} in terms of the Coulomb friction is defined as

$$|\mathbf{f}_{fric}| = \mu_{fric}m|\mathbf{a}_n|, \quad (51)$$

where μ_{fric} is the dynamic coefficient of friction. We could also easily implement the effect of a static friction coefficient, but we decided to use exclusively the dynamic one, since there is high uncertainty in obtaining such parameters.

Given that the corrected velocity \mathbf{v}'' is already parallel to the wall surface, we can finally derive \mathbf{f}_{fric} in both amplitude and direction as

$$\mathbf{f}_{fric} = \begin{cases} -\mu_{fric}m|\mathbf{a}_n|\frac{\mathbf{v}''}{|\mathbf{v}''|}, & \text{if } |\mathbf{f}_{fric}| < m|\mathbf{v}''|/\Delta t \\ -m|\mathbf{v}''|/\Delta t, & \text{otherwise.} \end{cases} \quad (52)$$

In other words, already exchanging the parameters \mathbf{a}_n and \mathbf{f}_{fric} by their definitions (Eqs. (50) and (51)), the newly corrected velocity \mathbf{v}''' due to friction can be defined as

$$\mathbf{v}''' = \begin{cases} \mathbf{v}'' - \mu_{fric}|\mathbf{n} \cdot \mathbf{v}'|\frac{\mathbf{v}''}{|\mathbf{v}''|}, & \text{if } \mu_{fric}|\mathbf{n} \cdot \mathbf{v}'| < |\mathbf{v}''| \\ 0, & \text{otherwise.} \end{cases} \quad (53)$$

Finally, the corrected soil particle velocity is retrieved as

$$\mathbf{v} = \mathbf{v}''' + \mathbf{v}_{\text{wall}}. \quad (54)$$

To increase clarity, algorithm 1 shows how this procedure is conducted step-by-step. Consider the target particle i in position \mathbf{x}_i approaching a wall particle in position \mathbf{x}_j with normal direction \mathbf{n}_j . If the distance between them is smaller than d and the relative velocity \mathbf{v}'_{ij} points to the wall, penetration is detected. Then, for the nearest wall particle j , correct the relative velocity (Eqs. (49) and (53)) and retrieve the corrected soil particle velocity (Eq. (54)).

The value of μ_{fric} might also be applied to impose some specific boundary conditions. For example, $\mu_{fric} = 0$ can be applied for a free-slip condition, while an infinite value (i.e., imposing $\mathbf{v}''' = 0$) for non-slip. In general situations, we consider $\mu_{fric} = \tan \phi$, where ϕ is the material internal friction angle.

Algorithm 1 Boundary conditions

Input: Target particle i : \mathbf{x}_i , \mathbf{v}_i , wall particles j : \mathbf{x}_j , \mathbf{v}_j , \mathbf{n}_j

Output: corrected velocity \mathbf{v}

if i is in the essential boundary domain **then**

 Impose essential boundary condition

else

for all wall neighbor particles j **do**

if $\text{dist}(\mathbf{x}_i, \mathbf{x}_j) \leq d$ & $\mathbf{v}'_{ij} \cdot \mathbf{n}_j \leq 0$ **then**

 Penetration detected.

 Check minimum $\text{dist}(\mathbf{x}_i, \mathbf{x}_j)$

end if

end for

for nearest penetrated wall particle j **do**

 Correct velocity for non-penetration condition: Eq. (49)

 Correct velocity for friction: Eq. (53)

 Retrieve corrected velocity: Eq. (54)

end for

end if

6.3. SPH approximations

The equations introduced in this section suppress the superscript for time to facilitate visualization, since it is clearly discernible from the context. For instance, a SPH approximation of the divergence of a variable in time β should use such variable in time β . Also, the so-called numerical density in SPH approximations are taken as the soil skeleton density (not the mixture density), since we are solving all equations in terms of soil Lagrangian particles. For example, the numerical density of a particle i is

$$\rho_i = (1 - n_i)\rho_s, \quad (55)$$

and its mass is

$$m_i = \rho_i d^3, \quad (56)$$

where d^3 is the particle volume.

In the predictor step (Eq. (46)), the divergence of effective stress is evaluated using Eq. (43)

$$\langle \nabla \cdot \boldsymbol{\sigma}' \rangle_i = \rho_i \sum_{j=1}^N m_j \left(\frac{\boldsymbol{\sigma}'_i}{\rho_i^2} \bar{\nabla} W(\mathbf{r}_{ij}, h) - \frac{\boldsymbol{\sigma}'_j}{\rho_j^2} \bar{\nabla} W(\mathbf{r}_{ji}, h) \right), \quad (57)$$

and the Laplacian of velocity for the JST stabilization term with Eq. (45) as

$$\langle \nabla^2 \mathbf{v} \rangle_i = \frac{2}{\rho_i} \sum_{j=1}^N m_j \frac{\mathbf{r}_{ij} \cdot \nabla W(\mathbf{r}_{ij}, h)}{\mathbf{r}_{ij}^2} (\mathbf{v}_i - \mathbf{v}_j), \quad (58)$$

while the convection term for the water predictor step (Eq. (22)) with Eq. (40)

$$\langle \nabla \otimes \mathbf{v}_w \rangle_i = \frac{1}{\rho_i} \sum_{j=1}^N m_j \tilde{\nabla} W(\mathbf{r}_{ij}, h) \otimes (\mathbf{v}_{w,j} - \mathbf{v}_{w,i}), \quad (59)$$

$$\langle (\mathbf{v} \cdot \nabla) \mathbf{v}_w \rangle_i = \mathbf{v}_i \cdot \langle \nabla \otimes \mathbf{v}_w \rangle_i. \quad (60)$$

Similarly, Eq. (40) is also used for the Jaumann rate stress update in Eq. (33) as

$$\langle \nabla \otimes \mathbf{v} \rangle_i = \frac{1}{\rho_i} \sum_{j=1}^N m_j \tilde{\nabla} W(\mathbf{r}_{ij}, h) \otimes (\mathbf{v}_j - \mathbf{v}_i). \quad (61)$$

Pressure gradient from the corrector step (Eq. (25)) is evaluated using equation Eq. (43)

$$\langle \nabla \cdot p \rangle_i = \rho_i \sum_{j=1}^N m_j \left(\frac{p_i}{\rho_i^2} \tilde{\nabla} W(\mathbf{r}_{ij}, h) - \frac{p_j}{\rho_j^2} \tilde{\nabla} W(\mathbf{r}_{ji}, h) \right), \quad (62)$$

Eq. (40) is also used to approximate both the divergence of predictor velocity in the PPE (Eq. (26)) and the evolution of porosity in Eq. (15)

$$\langle \nabla \cdot \mathbf{v} \rangle_i = \frac{1}{\rho_i} \sum_{j=1}^N m_j (\mathbf{v}_j - \mathbf{v}_i) \cdot \tilde{\nabla} W(\mathbf{r}_{ij}, h), \quad (63)$$

and

$$\langle \nabla \cdot \mathbf{v}_w \rangle_i = \frac{1}{\rho_i} \sum_{j=1}^N m_j (\mathbf{v}_{w,j} - \mathbf{v}_{w,i}) \cdot \tilde{\nabla} W(\mathbf{r}_{ij}, h), \quad (64)$$

Finally, the Laplacian of pressure for Eq. (26) is evaluated through Eq. (45)

$$\langle \nabla^2 p \rangle_i = \frac{2}{\rho_i} \sum_{j=1}^N m_j \frac{\mathbf{r}_{ij} \cdot \nabla W(\mathbf{r}_{ij}, h)}{\mathbf{r}_{ij}^2} (p_i - p_j). \quad (65)$$

6.4. Initial conditions

As usual in Geomechanics numerical simulations, the proposed method requires an initial condition for the effective stress distribution in the soil skeleton. Such initial condition might be evaluated through in-site measurements, or by other methods such as the one explained in Bui and Fukagawa (2013), for example. However, given that the purpose of this paper is to introduce the formulation rather than showing accurate applications, we simplify this assessment under the assumption that the program itself generate a reasonable effective stress distribution after a number of iterations.

More specifically, we start the simulation with a zero stress and zero velocity for all particles (unless otherwise predefined) and run the stress update, predictor step for the soil phase and apply the boundary condition a number of iterations, say, I_{init} iterations (hence, we do not update particle position for this initial phase). At the end, the generated stress distribution is considered to be the initial condition and velocities are once more set to zero. Algorithm 2 shows this process.

Notice that this procedure is the same as running the proposed method for dry soils without updating position vectors \mathbf{x} . The fact that it is not necessary to update pressure is due to the implicit nature of the corrector step, which means that there is no need for an initial pressure profile to start the program.

Algorithm 2 Initial conditions

Input: Initial \mathbf{x}, \mathbf{v} for all particles

Output: Effective stress distribution at the initial state σ'

Calculate kernel gradient correction (Eq. (42))

Assign $\sigma' = 0$ for all particles

for I_{init} iterations **do**

Calculate the soil predictor step (Eqs. (46), (57), (47) and (58))

Impose boundary condition (algorithm 1)

Update trial effective stress (Eq. (35))

Return mapping (algorithm 4)

end for

Reset velocity as $\mathbf{v} = 0$ for all particles

7. Proposed method overview

We have already explained all features of the proposed method in details. Now, we devote this section to facilitate understanding and provide a guideline for those who desire to reproduce it. Algorithm 3 shows in a step-by-step manner all procedure of this proposed method.

Here, Δt is restricted by a simple Courant–Friedrichs–Lewy (CFL) condition as

$$\Delta t \leq C_{CFL} \frac{d}{c_p}, \quad (66)$$

which the parameter $C_{CFL} = 0.5$ showed to be sufficient in our numerical tests.

Algorithm 3 Proposed method overview

Input: Initial \mathbf{x}, \mathbf{v} for all particles

Output: $\mathbf{x}, \mathbf{v}, \sigma', p$ and n for all particles after I iterations

Define Δt restricted by (66)

Initial effective stress state as algorithm 2

Initiate $\beta = 0$

for I iterations **do**

a) Calculate kernel gradient correction (Eq. (42))

b) Predictor step (Eqs. (46), (47), (57) and (58))

c) Predictor step for water phase (Eqs. (22), (59) and (60))

d) Impose boundary condition (algorithm 1)

e) Solve PPE (Eqs. (26), (27), (63) and (65))

f) Corrector step (Eqs. (25) and (62))

g) Impose boundary condition (algorithm 1)

f) Update porosity (Eqs. (15) and (63))

h) Update trial effective stress (Eq. (35))

if elastic body, $\sigma'^{t+1} = \sigma'^{\text{trial}}$ and **goto j**

i) Return mapping (algorithm 4 or 5)

j) Update position (Eq. (28))

k) New time iteration: $\beta = \beta + 1$

end for

8. Numerical examples

Here we give a couple of numerical tests to demonstrate the robustness of the proposed method. First, we verify the strong coupling $\mathbf{u} - \mathbf{w} - p$ formulation with a hydrostatic problem. Then, with 1D Terzaghi consolidation tests, we compare the three time integration schemes for the drag force as explained in Section 3 and assess its the sensitivity related to time increment and permeability. Following, we show the capability of the proposed method to simulate both drained and undrained conditions in a triaxial compression test with the modified Cam–Clay yield criterion. Finally, we show the applicability of this method using the Selborne slope failure experiment (Cooper et al., 1998) as a validation test in real scale.

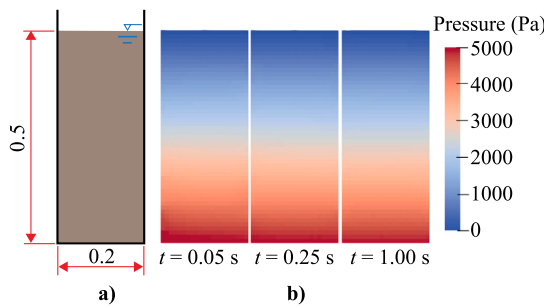


Fig. 4. Hydrostatic test: (a) geometry and (b) snapshots of the numerical test for different time steps showing the pressure profile.

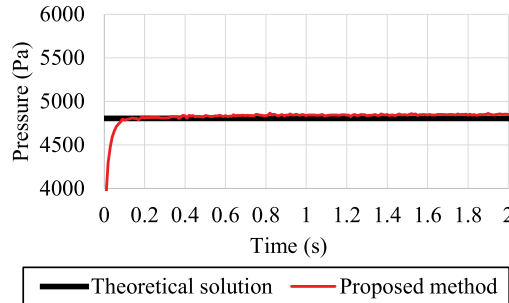


Fig. 5. Hydrostatic test: pressure as a function of time at the bottom center particle.

Unless otherwise said, the JST coefficient is taken as $\epsilon^{(2)} = 0.5$ for particles under elastic deformation and $\epsilon^{(2)} = 0.01$ for particles under plastic deformation.

8.1. Hydrostatic pressure

Here, we present a very simple verification test to check whether the current formulation is capable of generating hydrostatic pressure field. Although this test seems to be obvious at first glance, it is well-known in SPH community that SPH has some difficulties in dealing with static bodies due to the dynamic nature of the Lagrangian particles.

The fully saturated material is confined into a squared container as illustrated in Fig. 4a, and the parameters for this numerical test are listed in Table 1. Mohr–Coulomb model is taken in its perfectly plastic form. For the boundary conditions, all particles at either bottom or side walls are set $v_w = 0$, and $p = 0$ is enforced at the free-surface. We applied the natural boundary condition for v with $\mu_{fric} = \tan \phi$ for all walls.

Fig. 4b illustrates some snapshots at different time steps and Figs. 5 and 6 show a graphical summary of our results. From the graphical results, we conclude that our proposed method is capable of generating a smooth and stable hydrostatic pressure distribution over an extended period of time, as well as an almost indistinguishable pressure profile from the theoretical solution.

8.2. One-dimensional Terzaghi consolidation

The one-dimensional Terzaghi consolidation problem is probably to most widely used benchmark test in Geomechanics. It consists in a tall container filled with saturated soil, and a constant stress applied on the top free-surface. Here, we selected the same model parameters as Bandara and Soga (2015), that is, a squared container 1 m tall and 0.06 m wide, as illustrated in Fig. 7a. The simulation is started with both pressure and effective stress set to 0, and the other parameters are listed in Table 2. Exceptionally, the JST constant $\epsilon^{(2)}$ is set to 0.

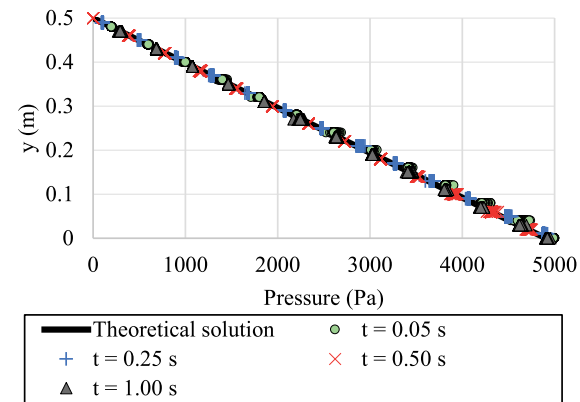


Fig. 6. Hydrostatic test: graphical representation of pressure profile at different time steps.

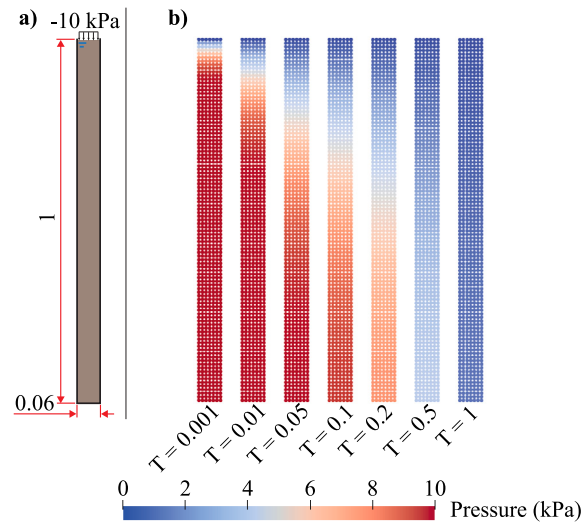


Fig. 7. Terzaghi consolidation problem: (a) geometry (in m) and (b) snapshots of the resulting numerical simulation for $k = 10^{-3} \text{ m/s}$ and $\Delta t = 10^{-5} \text{ s}$ at different time steps showing the pressure profile.

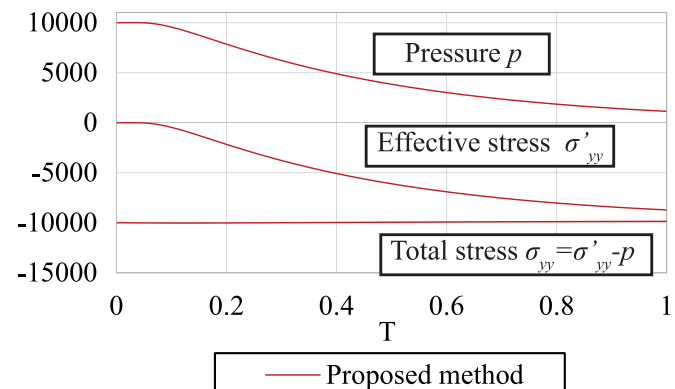


Fig. 8. Terzaghi consolidation problem: average values of effective stress, pressure and total stress in relation to time factor T on the second layer of particles from bottom to top for $k = 10^{-3} \text{ m/s}$ and $\Delta t = 10^{-5} \text{ s}$.

The gravity effect is neglected, that is, $\mathbf{g} = 0$, although the scalar g is maintained as 9.81 m/s^2 in the drag force. To get the best accuracy

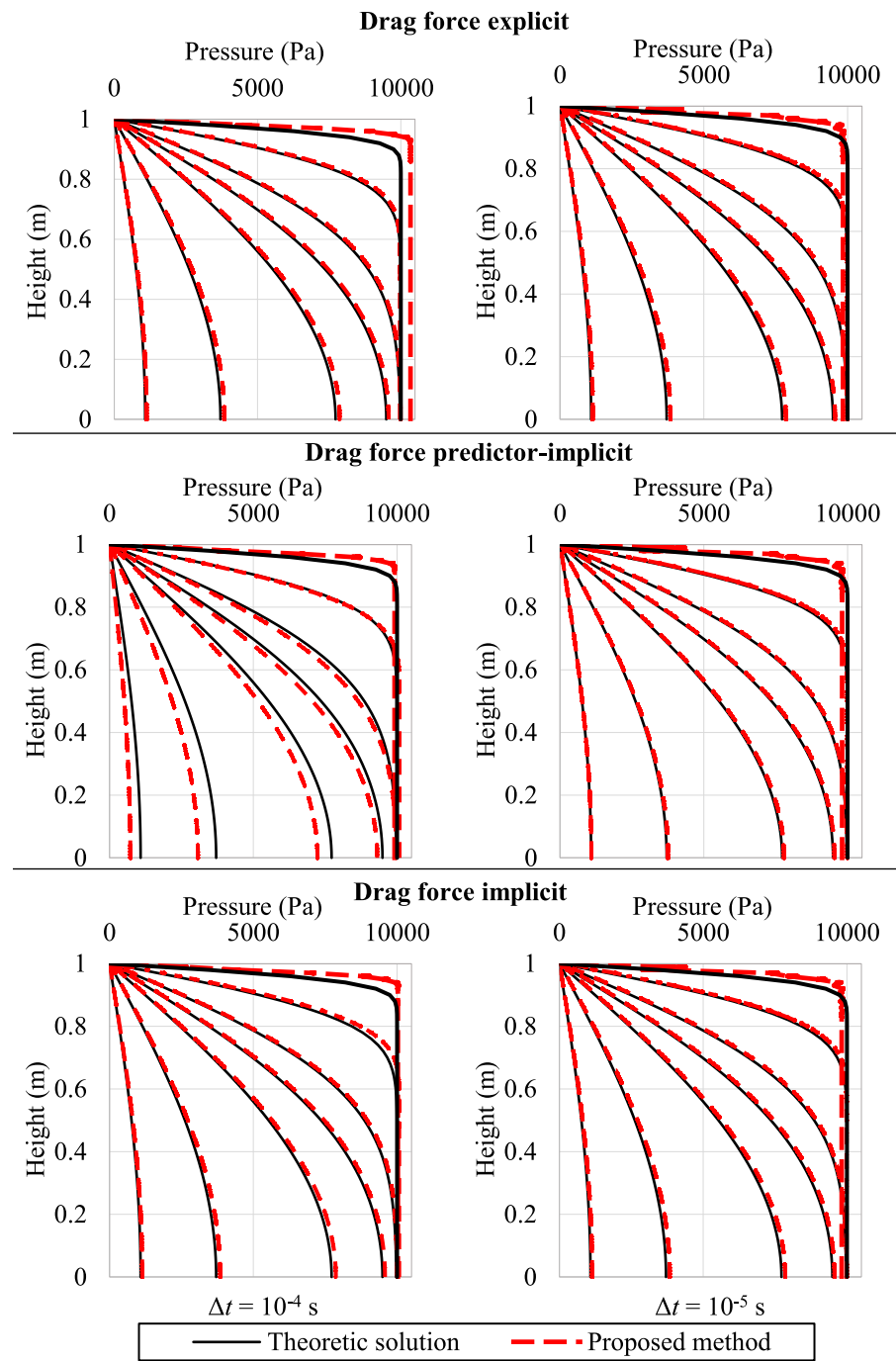


Fig. 9. Terzaghi consolidation problem: pressure profiles compared to the theoretical solution with $k = 10^{-3}$ m/s, $\Delta t = 10^{-4}$ s (left) and $\Delta t = 10^{-5}$ s (right) at $T = 0.001$, $T = 0.01$, $T = 0.05$, $T = 0.1$, $T = 0.2$, $T = 0.5$ and $T = 1$.

possible, all boundary conditions are treated as essential boundary conditions. They are:

- $\mathbf{v} = \mathbf{v}_w = \mathbf{0}$ at the bottom;
- $\mathbf{v}_w = \mathbf{0}$ at the side walls (impermeable walls and no-slip condition);
- \mathbf{v} in the normal direction of the wall is zero at the side walls (no-penetration);
- $p = 0$ at the free-surface.

Lastly, the upper stress of -10 kPa is applied at the free-surface particles in the form of an acceleration

$$a_{1D} = -\frac{10000}{d(1-n)\rho_s}, \quad (67)$$

in the y direction included in the predictor step of the soil linear momentum equation, Eq. (46). As usual for this experiment, we present the results in function of a dimensionless time parameter T , called time factor, defined as

$$T = \frac{km_v}{\rho_w g H^2} t, \quad (68)$$

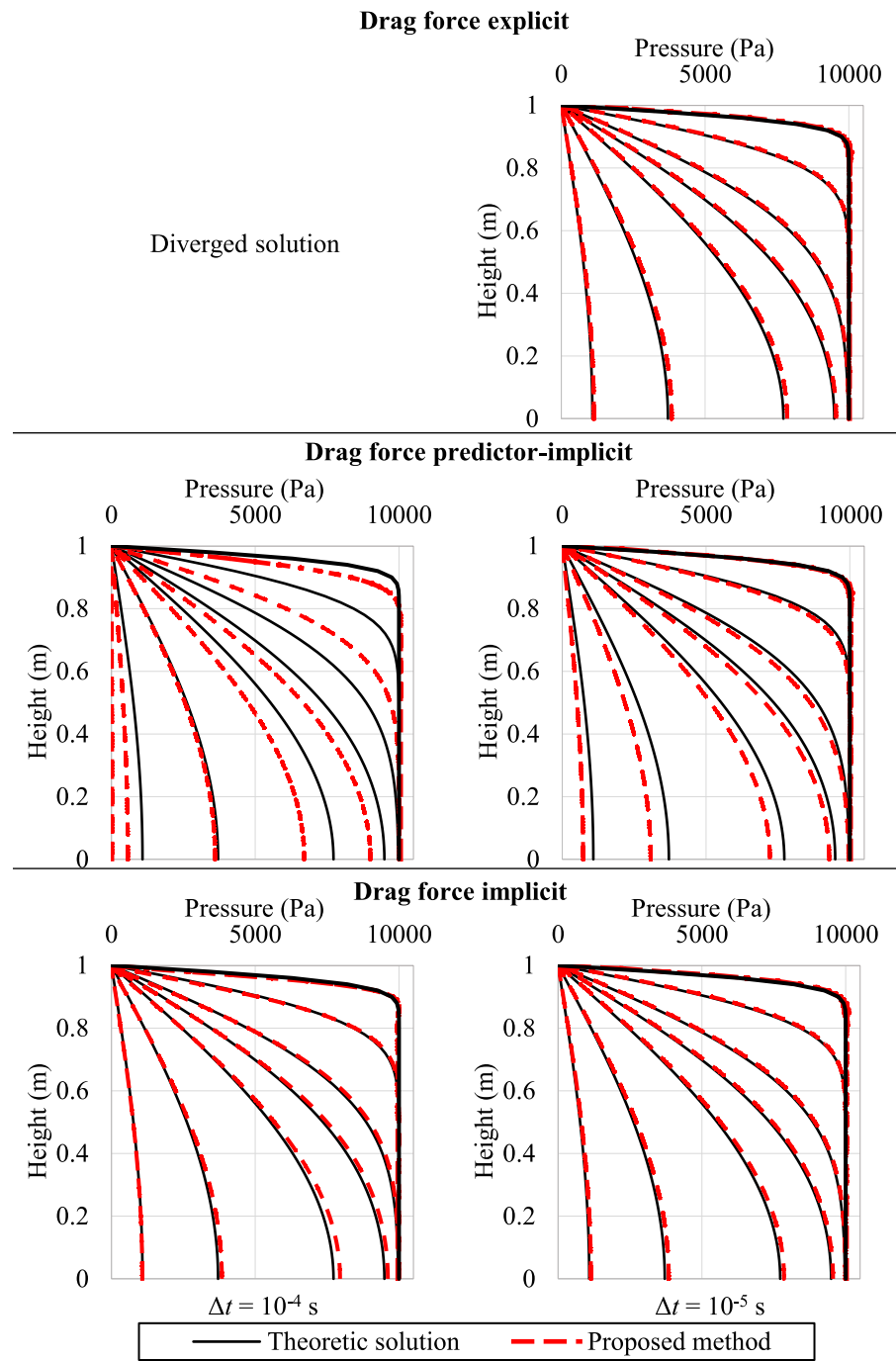


Fig. 10. Terzaghi consolidation problem: pressure profiles compared to the theoretical solution with $k = 10^{-4}$ m/s, $\Delta t = 10^{-4}$ s (left) and $\Delta t = 10^{-5}$ s (right) at $T = 0.001$, $T = 0.01$, $T = 0.05$, $T = 0.1$, $T = 0.2$, $T = 0.5$ and $T = 1$.

where

$$m_v = \frac{E(1-\nu)}{(1+\nu)(1-2\nu)}, \quad (69)$$

is the constrained modulus and H the height of the specimen.

Fig. 7 shows some snapshots of this numerical test and Fig. 8 the average stress values as a function of time at the second layer of particles from bottom to top. From Fig. 8, it is possible to conclude that the pressure dissipation followed by the effective stress increase acts almost exactly the same as the theory demands, that is, the total stress $\sigma'_{yy} - p$ is maintained as the applied vertical stress (-10 kPa) throughout the whole process.

Next, we show an analysis of the sensitivity of the proposed method in relation to the time increment Δt and permeability k . Figs. 9 and 10 show the pressure profiles for different times comparing the “drag force explicit” (as in Eq. (19)), “drag force predictor-implicit” (as in Eq. (21)) and “drag force implicit” (proposed method) schemes, as explained in Section 3.

We hypothesize that the accuracy and stability of the method is directly linked to the scalar multipliers of the drag force, here denoted as a and b in Eq. (20), especially for the “drag force explicit” case. Supporting this idea, for example, the solutions with the “drag force explicit” scheme are accurate for $k = 10^{-3}$ m/s and $dt = 10^{-4}$ s, where both parameters are lower than 1 ($a = 0.0476$ and $b = 0.294$),

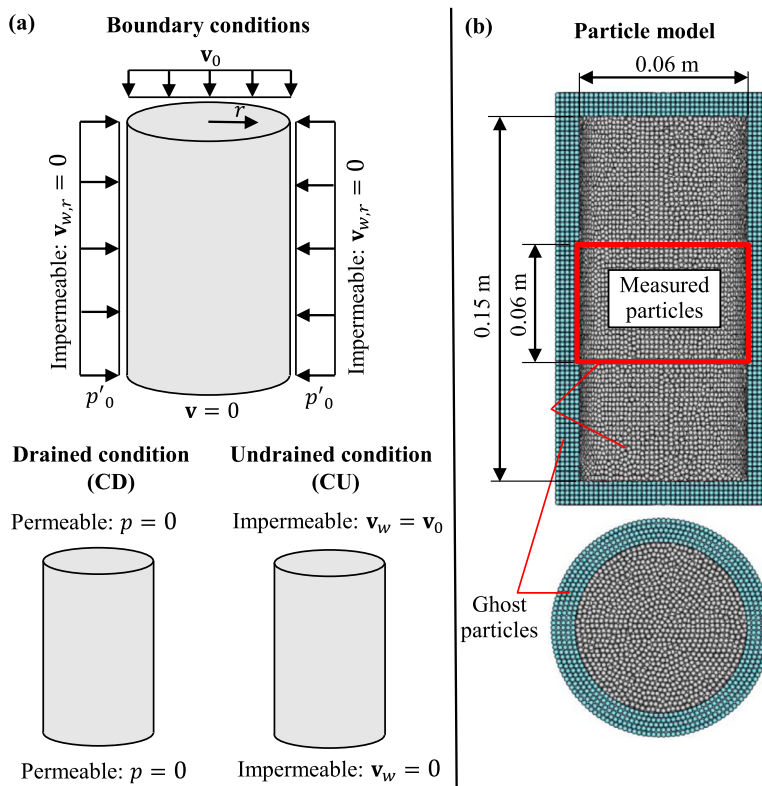


Fig. 11. Triaxial compression: (a) boundary conditions and (b) particle model.

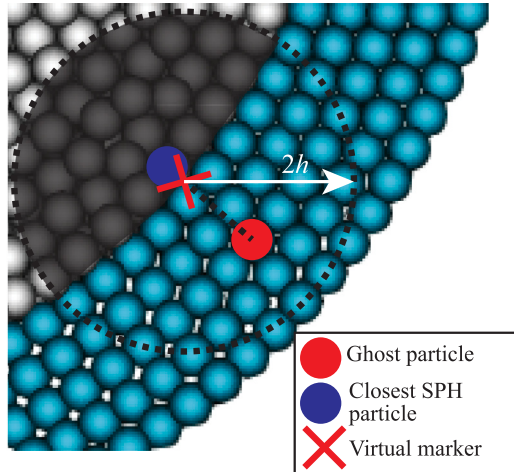


Fig. 12. Triaxial compression: elements to define the velocity of lateral ghost particles.

while it diverges the solution for $k = 10^{-4}$ m/s and $dt = 10^{-4}$ s, since $b = 2.943 > 1$.

Between the three time integration methods, the “drag force predictor-implicit” seems to be the most influenced by this constraint in terms of accuracy, given that the only solution with comparable accuracy was the one with $k = 10^{-3}$ m/s and $dt = 10^{-5}$ s ($a = 0.0048$ and $b = 0.0294$). On the other hand, it solves the problem present in the “drag force explicit” scheme of having the numerical test being diverged, as it can be seen in the simulation with $k = 10^{-4}$ m/s and $dt = 10^{-4}$ s ($a = 0.48$ and $b = 2.943$). It is important to mention that (Kularathna et al., 2021) was able to have very accurate solutions with the “drag force predictor-implicit” time integration scheme, which might be due to the their fractional-step algorithm or other specificity in their MPM formulation. Finally, with this example we demonstrated

Table 1
Material and numerical parameters of the hydrostatic test.

Parameter	Symbol	Value
Young's modulus	E	10 MPa
Poisson's ratio	ν	0.3
Soil density	ρ_s	2800 kg/m ³
Cohesion	c	0
Friction angle	ϕ	30°
Dilatancy angle	ψ	0°
Initial porosity	n_0	0.3
Water density	ρ_w	1000 kg/m ³
Permeability	k	10 ⁻³ m/s
Time increment	Δt	10 ⁻⁵ s
Particle size	d	0.01 m
Iterations at initial state	I_{init}	1000
Constitutive model		Mohr-Coulomb

Table 2
Material and numerical parameters of the Terzaghi consolidation test.

Parameter	Symbol	Value
Particle diameter	d	0.01 m
Young's modulus	E	10 MPa
Poisson's ratio	ν	0.3
Soil density	ρ_s	2650 kg/m ³
Initial porosity	n_0	0.3
Water density	ρ_w	1000 kg/m ³
Permeability	k	10 ⁻³ m/s
Constitutive model		Purely elastic

that the “drag force implicit” integration scheme was the most robust among them, leading to accurate solutions for all pairs of Δt and k .

8.3. Triaxial compression

The triaxial compression test is a classical physical experiment widely used in Soil Mechanics. A few studies such as Pereira et al.

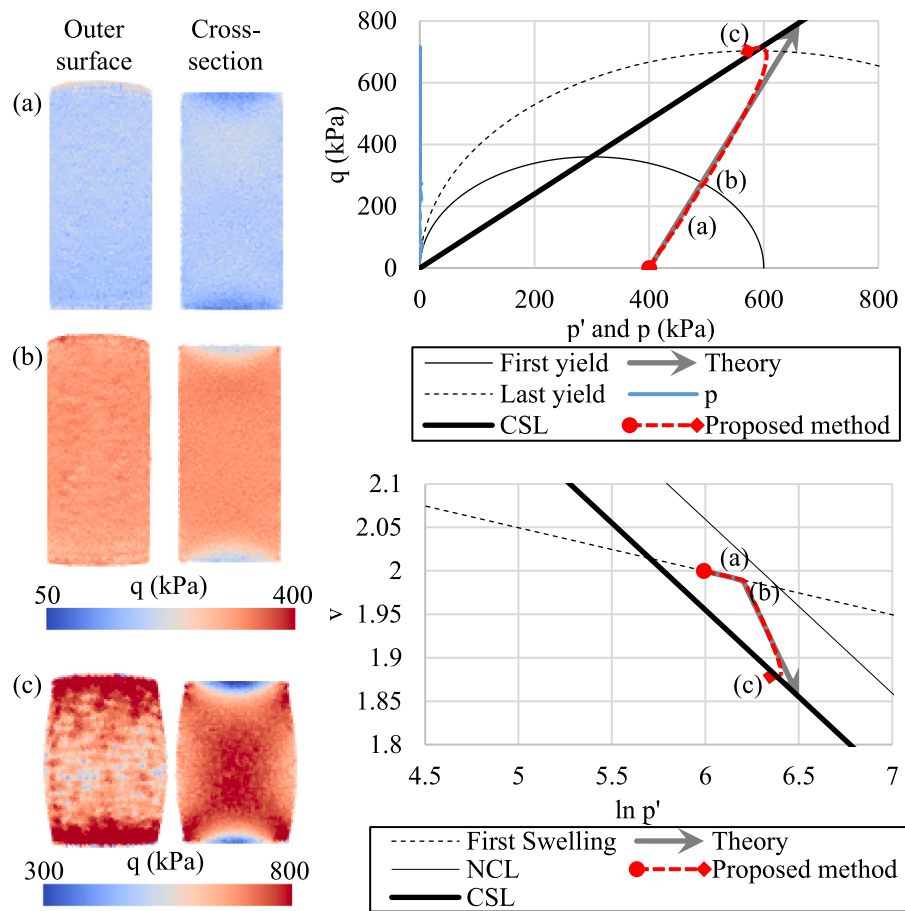


Fig. 13. Triaxial compression, CD-L: snapshots of the resulting numerical simulation showing the von Mises stress at the outer surface and centered cross section at half-way to start yielding (a), right after yielding (b) and closest point to CSL (c) (left) and graphical representation of the (p', q) and $(\ln p', v)$ spaces (right).

(2017) and Zhao et al. (2019) have successfully used SPH to simulate it. The former used Drucker–Prager and the latter, Mohr–Coulomb yield criteria. Here we selected the modified Cam–Clay, as it is greatly considered appropriate for this problem. In addition, both Pereira et al. (2017), Zhao et al. (2019) have considered an uncoupled problem, which means that their solutions resemble the drained condition. In this work, we devote special attention on using the proposed method to simulate both drained and undrained conditions.

Fig. 11a shows the boundary conditions for the triaxial test. The main difficulty in simulating this problem with SPH is the lateral boundary condition, which can move sideways freely while maintaining a constant confining pressure. Both Pereira et al. (2017), Zhao et al. (2019) simulated this condition with additional forces applied to the SPH particles representing the specimen itself. As shown in Fig. 11b, we chose to use ghost particles to simulate all boundary conditions, since it is easier to arrange the conditions on the water phase.

In short, the ghost particles at the bottom are stationary while those at the top have a constant velocity $v_0 = -0.1$ m/s at the vertical direction. The lateral ghost particles, on the other hand, are assigned with a virtual marker located at the interface between the SPH specimen particles and the ghost particles, as shown in Fig. 12. Then, its effective stress is kept constant as $\sigma' = p'_0 \mathbf{I}$, and its velocity is determined as

$$\mathbf{v}_g = \gamma \mathbf{v}_{out} + (1 - \gamma) \frac{\sum_{j=1}^{N_s} \frac{m_j}{\rho_j} \mathbf{v}_j W(\mathbf{r}_{ij}, h)}{\sum_{j=1}^{N_s} \frac{m_j}{\rho_j} W(\mathbf{r}_{ij}, h)}, \quad (70)$$

where \mathbf{v}_{out} is the velocity of the closest specimen particle to the virtual marker as represented in Fig. 12, and the second term is the SPH approximation (Eq. (36)) only at the soil specimen particles corrected for the absence of a complete kernel. The proportion parameter γ was incorporated based on the fact that using exclusively \mathbf{v}_{out} makes the simulation unstable, while using only the average velocity results in an additional strong stiffness in the lateral boundary. From experience, $\gamma = 0.8$ resulted in the best solutions.

In addition to the definitions on Fig. 11a, we selected a very large value of permeability k for drained and very low for undrained conditions to adapt our simulation to these conditions. However, the undrained condition leads to a situation where there is no Dirichlet condition on pressure, which makes the PPE to not converge. To fix that, we assign zero pressure to the outermost layer of lateral ghost particles. As of the initial configuration, we started the simulation with all particles with $\sigma' = p'_0 \mathbf{I}$, zero pressure and velocity and slightly randomly distributed particles (as in Fig. 11). Similarly to the previous example, gravity is neglected.

Table 3 summarizes the parameters adopted in this simulation. The specimen is a cylinder with 0.06 m of diameter and 0.15 m height. To facilitate the notation, we are going to refer to CD as the drained and CU as the undrained tests. L represents lightly consolidated and H, highly consolidated. Figs. 13–16 show the graphical results of the (p', q) and $(\ln p', v)$ spaces and the simulations at three different stages: (a) half-way to start yielding, (b) right after yielding and (c) the closest point to the critical state line. The stresses and specific volume ($v = 1 + n/(1 - n)$) are taken as the average of the particles located in the mid of the specimen (as in Fig. 11b). Notice that p' is calculated

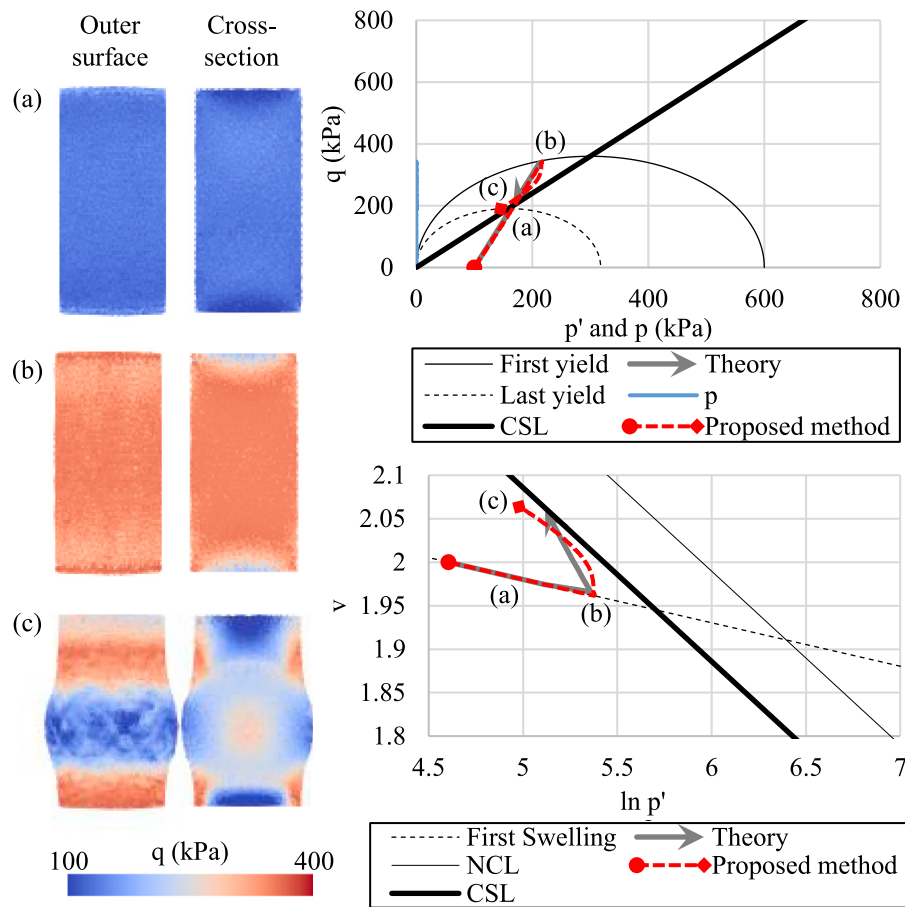


Fig. 14. Triaxial compression, CD-H: snapshots of the resulting numerical simulation showing the von Mises stress at the outer surface and centered cross section at half-way to start yielding (a), right after yielding (b) and closest point to CSL (c) (left) and graphical representation of the (p', q) and $(\ln p', v)$ spaces (right).

as positive for tension (as in algorithm Appendix B) but exhibited as positive for compression to show it in the most familiar representation in the Geomechanics community.

As expected, the proposed method results are reasonable in comparison with the theoretical solution for the stress path, that is, following a straight line with slope of 1:3 ($p' : q$) for CD, while being a straight vertical line at the (p', q) space before yielding for CU. In addition, it is possible to conclude that the water pressure p also behaves naturally, being almost null for CD and absorbing the stresses that were not contained in p' for CU.

Solutions were also very close to the theoretical solution for the $(\ln p', v)$ space, following the swelling line before yielding for CD and being basically incompressible for CU. For completeness, we plot the stress-strain curves of our simulations in Fig. 17, which also shows reasonable solutions, approaching a horizontal line once it reaches the critical state line (CSL).

All results in this section were obtained with a particle size of $d = 0.002$ m. As a simple analysis of the convergence of the proposed method in relation to particle size, we conducted the CD-H numerical experiment for four different particle resolutions: 0.01, 0.005, 0.002 and 0.001 m. Fig. 18 shows these results in the (p', q) space. As expected, the numerical results approach the theoretical solution as particle size decreases.

The only major problem was a divergence of the solution once it approaches the CSL, which might be due to unsatisfactory boundary conditions. Although not perfect, we consider that the proposed method was successful in reproducing the triaxial compression test.

Table 3
Material and numerical parameters of the triaxial compression test.

Parameter	Symbol	Value
Particle size	d	0.002 m
Time increment	Δt	10^{-6} s
Gradient of swelling line	κ	0.05
Gradient of the normal consolidation line	λ	0.2
Poisson's ratio	ν	0.3
Soil density	ρ_s	3000 kg/m ³
Initial porosity	n_0	0.5
Water density	ρ_w	1000 kg/m ³
Drained permeability	k	10^{-1} m/s
Undrained permeability	k	10^{-8} m/s
Initial pre-consolidation pressure	p_c	600 kPa
Confining pressure for lightly consolidated soil	p'_0	400 kPa
Confining pressure for highly consolidated soil	p'_0	100 kPa
Constitutive model		Modified Cam-Clay

8.4. Slope failure with Selborne experiment

This final numerical example is to show an application to the proposed method in a realistic scale. Here, we reproduce the Selborne experiment (Bromhead et al., 1998; Cooper et al., 1998) using the Mohr-Coulomb constitutive model with softening linearly dependent on accumulated plastic strain. The geometry is illustrated in Fig. 19 and the parameters are summarized in Table 4 (values of porosity, Poisson's ratio and density are taken as usual values for clay). From the on-site investigations, Cooper et al. (1998) have identified four strata of soil, as shown in Fig. 19a. Given the deformation pattern from the experiment,

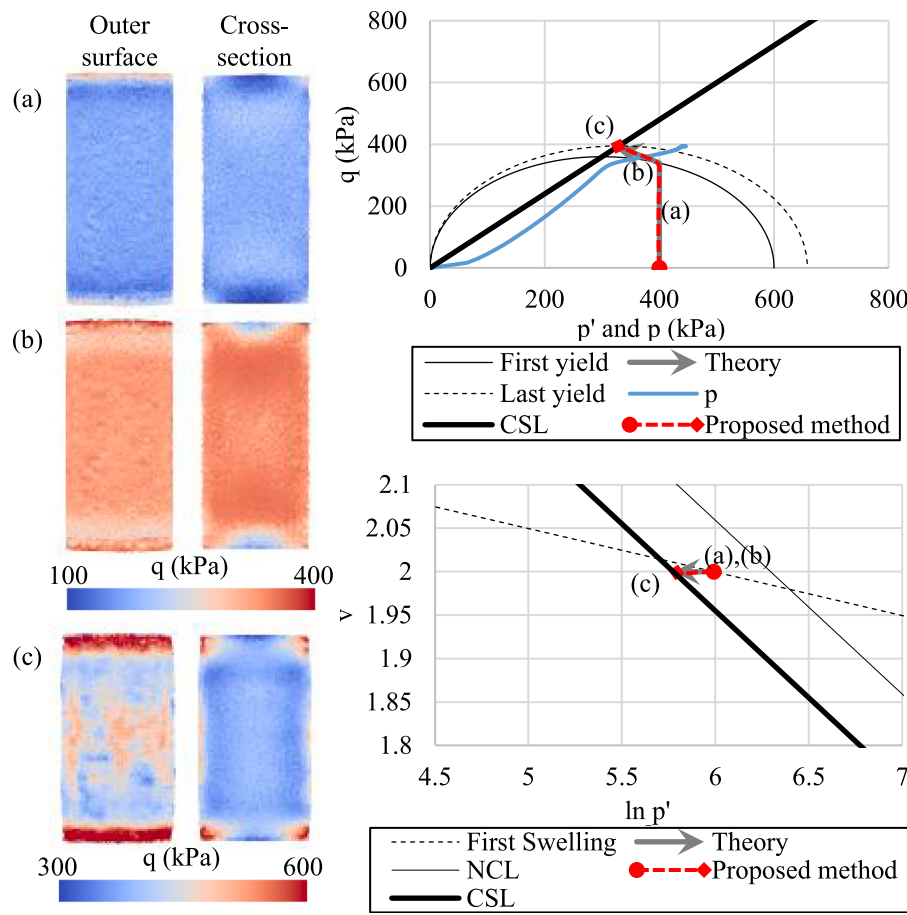


Fig. 15. Triaxial compression, CU-L: snapshots of the resulting numerical simulation showing the von Mises stress at the outer surface and centered cross section at half-way to start yielding (a), right after yielding (b) and closest point to CSL (c) (left) and graphical representation of the (p', q) and $(\ln p', v)$ spaces (right).

we decided to model this problem using only the three upper layers as indicated in Fig. 19b and c.

Initially, the slope had a smooth inclination as shown in Fig. 19a and it was later excavated to a 1:2 inclination. To approximate the initial condition on the effective stress, we conducted the initial steps (algorithm 2) including the excavated material shown in Fig. 19. Then, before starting the main loop, the excavated material is removed from the simulated domain.

Cooper et al. (1998) induced the slope failure through a recharge system that increased the pore pressure deep beneath the slope, as illustrated in Fig. 20a. The experiment lasted approximately 200 days, and they induced pore pressures of $p_0 = 30$ kPa, $p_0 = 42.5$ kPa, $p_0 = 53.5$ kPa and $p_0 = 70$ kPa, when it finally failed.

Based on Fig. 20a, we implemented the essential boundary conditions as illustrated in Fig. 20b, where p_0 represents the pore pressure induced in the experiment. In addition, the slope site was laterally isolated by low-friction panels to mimic a 2D problem. Hence, we modeled the boundary conditions on the furthermost lateral particles in a Dirichlet manner, enforcing v and v_w in the z direction as zero.

First, we checked the capability of the proposed method to induce the slope failure at the given $p_0 = 70$ kPa while predicting no failure for the smaller values. Fig. 21 shows the simulation results at $t = 50$ s for three cases: dry soil, saturated soil with $p_0 = 53.5$ kPa and saturated soil with $p_0 = 70$ kPa. As expected, slope failure was induced for the latter. For the dry case, basically no plastic deformations were found, while for $p_0 = 53.5$ kPa, one can see some plastic deformation at the interface of the induced pressure zone, but not enough to cause a catastrophic failure.

Table 4
Material and numerical parameters of the slope failure test.

Parameter	Symbol	Value
General parameters		
Particle size	d	0.5 m
Time increment	Δt	10^{-3} s
Iterations at initial state	I_{init}	2000
Water density	ρ_w	1000 kg/m ³
Young's modulus	E	20 MPa
Poisson's ratio	ν	0.4
Soil density	ρ_s	2000 kg/m ³
Initial porosity	n_0	0.5
Permeability	k	10^{-8} m/s
Dilatancy angle	ψ	0°
Constitutive model		Mohr–Coulomb
Soliflucted clay		
Peak cohesion	c	5 kPa
Residual cohesion	c_r	0
Friction angle	ϕ	21°
Weathered gault clay		
Peak cohesion	c	10 kPa
Residual cohesion	c_r	0
Friction angle	ϕ	24°
Unweathered gault clay		
Peak cohesion	c	25 kPa
Residual cohesion	c_r	0
Friction angle	ϕ	26°

It is very complicated to validate our results comparing it with the observed soil behavior in a quantitatively manner. Instead, we show some qualitative comparisons in Figs. 22 and 23.

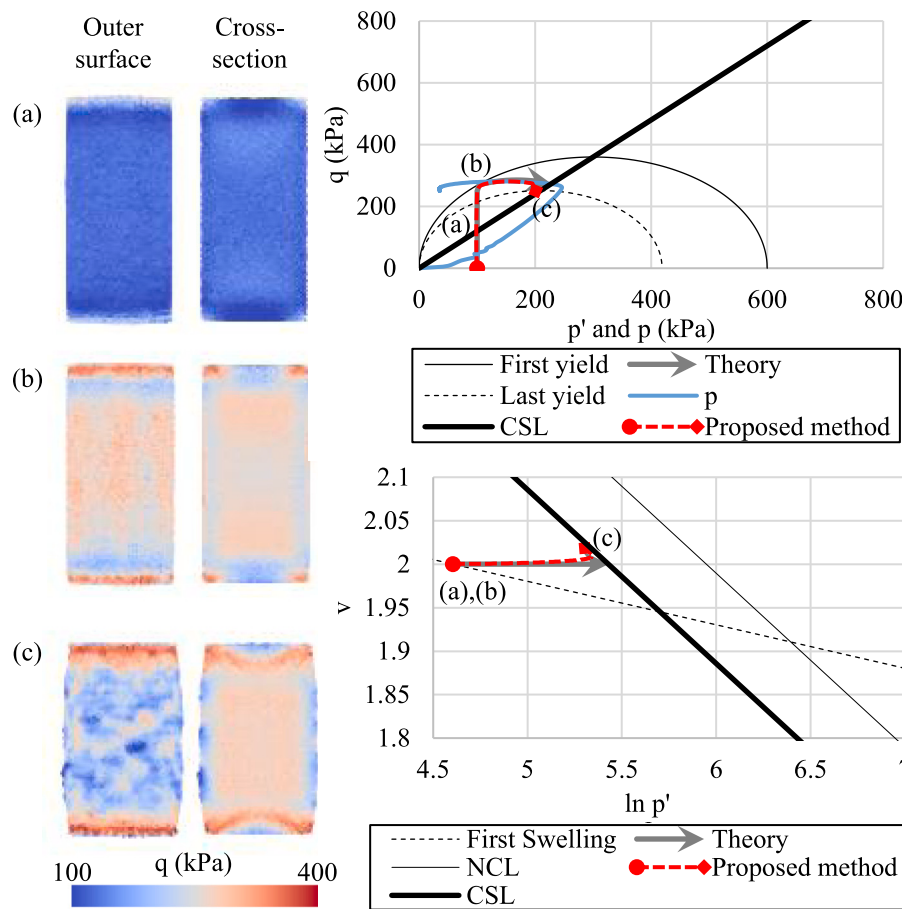


Fig. 16. Triaxial compression, CU-H: snapshots of the resulting numerical simulation showing the von Mises stress at the outer surface and centered cross section at half-way to start yielding (a), right after yielding (b) and closest point to CSL (c) (left) and graphical representation of the (p', q) and $(\ln p', v)$ spaces (right).

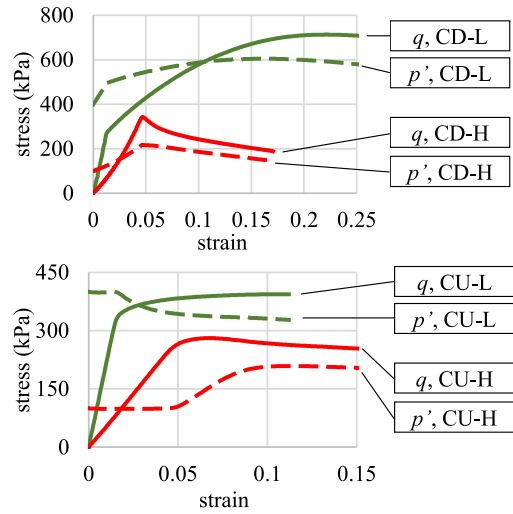


Fig. 17. Triaxial compression: graph of the stress-strain curve for all numerical simulations ($d = 0.002$ m).

In Fig. 22, the observed slip surface is plotted over our numerical simulations with colors indicating the accumulated plastic strain. The slip surfaces roughly coincide, although the observed one shows a more rounded and compact shape. In the numerical case, the slip surface follows the interface between the tougher unweathered gault clay layer and weaker weathered gault clay, which causes the seemingly straight

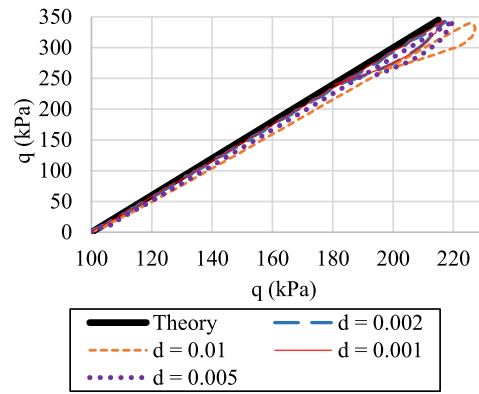


Fig. 18. Triaxial compression: graphical representation of the (p', q) space with a comparison of different particle sizes (particle sizes in m).

line at the right-side of the contour. Since the observed slip surface in the experiment is not a perfectly precise data and that its shape varies due to many uncertainties, we conclude that our simulation is able to reasonably predict this feature.

Next, Fig. 23 shows a picture taken after the slope collapse and the 3D view of our numerical solution. In the picture, Fig. 23a, it is possible to see that the soil mass slipped over the slip surface while the upper part roughly maintained its original shape. Similarly, as shown in Fig. 23b, our final numerical solutions with $p_0 = 70$ kPa can be divided into three types: undeformed particles (I), particles with high plastic

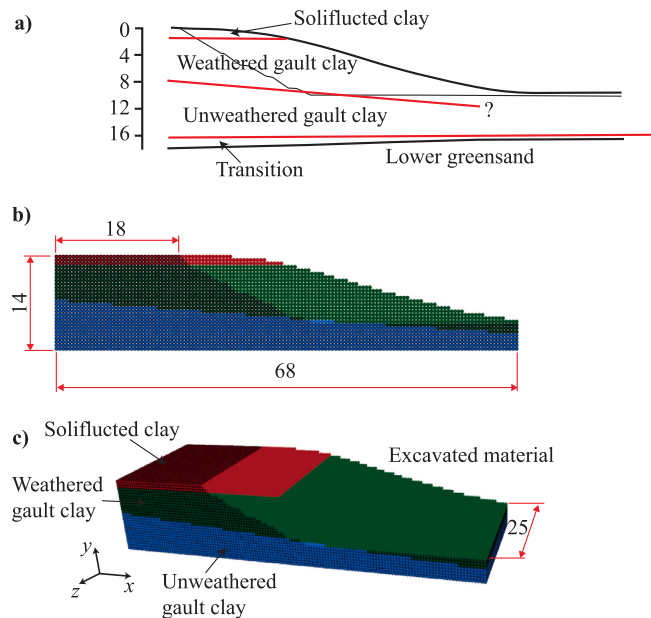


Fig. 19. Slope failure test: (a) actual cross section of the Selborne experiment as shown in Cooper et al. (1998) and the SPH particle model in (b) 2D and (c) 3D views (lengths in m).

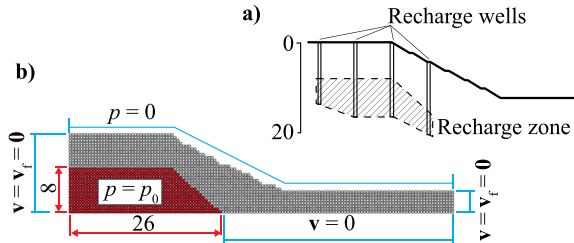


Fig. 20. Slope failure test: (a) Pore pressure recharge system as shown in Cooper et al. (1998) and (b) Dirichlet boundary conditions imposed in the SPH particle model (lengths in m).

deformation (II) and carried particles with low plastic deformation (III). Again, it is very complicated to accurately state in what degree our numerical solution follows the results found in Cooper et al. (1998). However, we believe that the resemblance presented in Fig. 23 is a fair evidence of the robustness of our proposed method.

For completeness, Fig. 24 shows some screenshots of our numerical simulation with $p_0 = 70 at several time steps. Pressure and vertical stress distributions seems to be fairly stable and smooth. The simulation extended up to 100 s, and there were no major modifications except for some numerical error accumulation.$

9. Conclusion

This paper presents a novel strong coupling technique for the $\mathbf{u} - p$ formulation based on an one point–two phases ISPH method for Geomechanics problems. The starting point is Biot's formulation (Biot, 1956) as explained in Zienkiewicz et al. (1999). Then, we further increase Mathematical consistency applying the complete incompressibility constraint on soil grains and pore water.

The formulation is then adapted to the ISPH projection scheme, resulting in a semi-implicit technique with strong coupling between soil and water phases. Darcy's drag force is updated implicitly to avoid large restrictions on time increment due to small values of permeability. We propose a simple yet robust boundary condition treatment where essential boundary conditions are simply enforced in a Dirichlet manner,

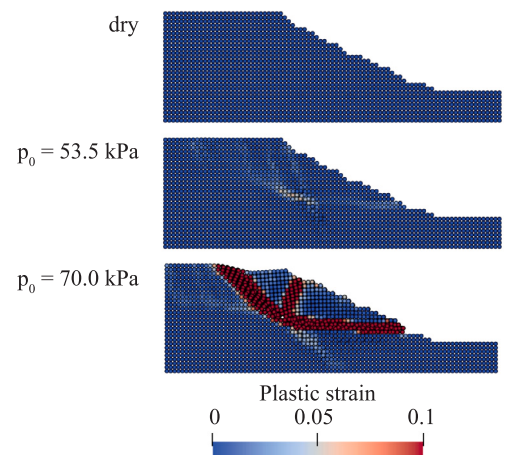


Fig. 21. Slope failure test: comparison between different induced pressure boundary conditions showing the accumulated plastic strain. Simulations at $t = 50$ s.

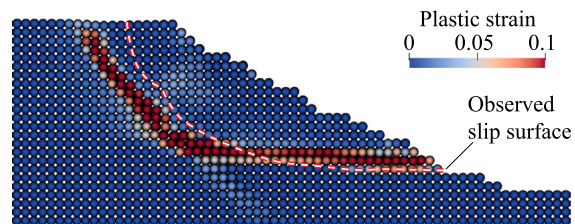


Fig. 22. Slope failure test: comparison between the interpreted slip surface found in Cooper et al. (1998) and the accumulated plastic strain at time $t = 11.5$ s ($p_0 = 70$ kPa case).

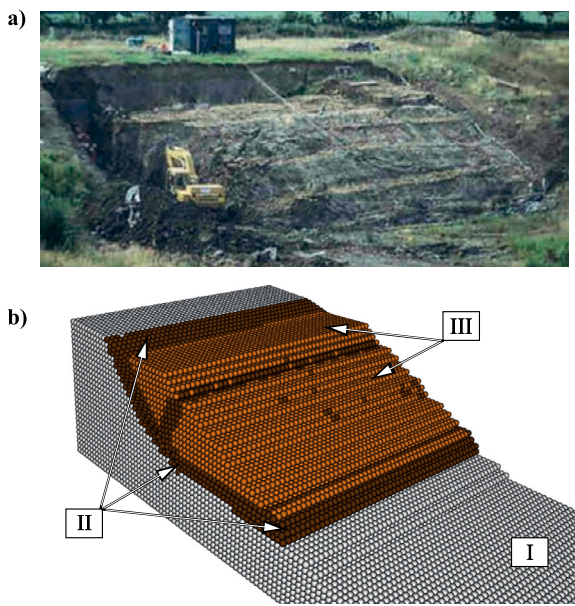


Fig. 23. Slope failure test: (a) picture of the slope after collapse (Bromhead et al., 1998) and (b) the SPH particle distribution at $t = 50$ s, where the white particles (I) represent the undeformed area, dark brown (II), particles with $\epsilon_p \geq 0.1$ and light brown (III), carried particles with $\epsilon_p < 0.1$ ($p_0 = 70$ kPa case).

while natural boundary conditions are applied in the form of velocity constraints, which include both non-penetration and friction effects.

We verified the strong coupling technique with hydrostatic and 1D Terzaghi consolidation. For both problems, we show exceptional

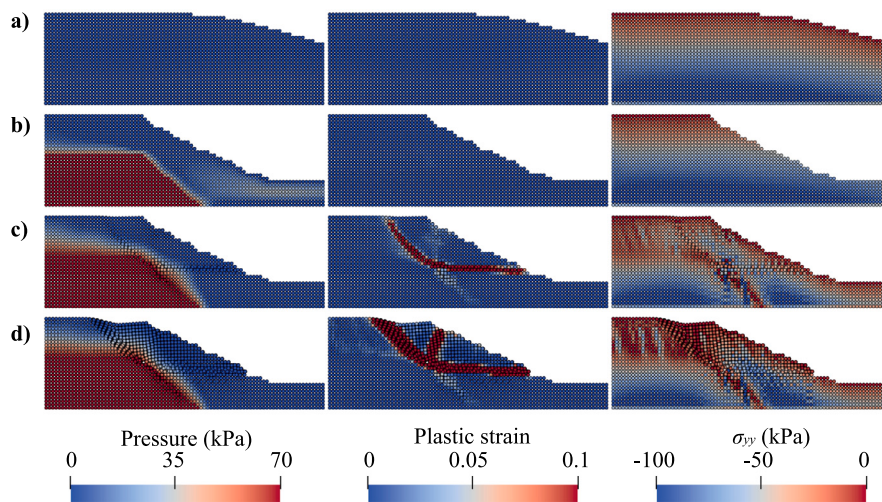


Fig. 24. Slope failure test: screenshots of the numerical simulation showing pressure, accumulated plastic strain and vertical stress at (a) $t = 0$ s, (b) $t = 10$ s, (c) $t = 11.5$ s and (d) $t = 50$ s ($p_0 = 70$ kPa case).

agreement with the theoretical values in terms of pressure profile as a function of height and pressure stability over time. Also, we demonstrated the capability of the proposed “drag force implicit” time integration of relieving the dependency of time increment in relation to the permeability.

Next, we demonstrated that our proposed method can simulate the triaxial compression test with the modified Cam–Clay yield criterion in both drained and undrained conditions for lightly and highly consolidated soils. The authors are unaware of any application of SPH soil–water coupling that can reproduce this problem at both drained and undrained conditions with this degree of fidelity.

Finally, we show the robustness of our proposed method with a numerical test based on the well-known Selborne experiment. We could model this experiment in a way that the slope failure occurs at the designated pore pressure induced in the experiment ($p_0 = 70$ kPa), while maintaining its stability for the second highest value ($p_0 = 53.5$ kPa). Then, we compared the shape of the slip surface and a 3D view of the failed soil mass with those obtained in the experiment, and we concluded that we could reasonably resemble what was observed. It is important to emphasize that this is not a rigorous validation test, since the exact conditions on the experiment are not given in a way that we could implement directly in the method. Hence, some model parameters and geometries had to be estimated, which might contribute to some degree of uncertainties. However, we consider that the simulation was successful, since our results were meaningful in a qualitative way.

As for future works, we intend to apply this method for more complex problems, which takes into account more complicated soil behavior such as soil under earthquake, liquefaction and so on. For the development of the method itself, we aim to expand its formulation to contemplate unsaturated soil behavior as well, which would allow us to simulate the water infiltration process, scouring and piping, as well as more realistic estimation of soil strength under a variety of scenarios.

CRediT authorship contribution statement

Daniel S. Morikawa: Conceptualization, Methodology, Software, Formal analysis, Investigation, Resources, Data curation, Writing – original draft, Writing – review & editing, Visualization, Project administration, Funding acquisition. **Mitsuteru Asai:** Methodology, Software, Formal analysis, Resources, Data curation, Writing – review & editing, Supervision, Project administration, Funding acquisition.

Declaration of competing interest

The authors declare that they have no known competing financial interests or personal relationships that could have appeared to influence the work reported in this paper.

Acknowledgments

The first author is supported by the Japan Society for the Promotion of Science (JSPS) through the Research Fellowship for Young Scientists.

This work was supported by the Japan Society for the Promotion of Science (JSPS) KAKENHI Grant Number 20J13114, JP-20H02418, 19H01098, and 19H00812. We also received computational environment support through the Joint Usage/Research Center for Interdisciplinary Large-scale Information Infrastructures (JHPCN) in Japan (Project ID: jh200034-NAH and jh200015-NAH).

Appendix A. Mohr–coulomb

Here we show the Mohr–Coulomb constitutive model with linear hardening rule on the cohesion variable. It is defined in terms of the principal stresses

$$\sigma' = \sum_{i=1}^3 \sigma_i \mathbf{e}_i \otimes \mathbf{e}_i, \quad (71)$$

and the plastic parameters are c (varying from initial c_0 to residual c_r values), ϕ and ψ . Yield function and flow rule are shown as follows.

- Yield function

$$\varphi = (\sigma_1 - \sigma_3) - (\sigma_1 + \sigma_3) \sin \phi - 2c \cos \phi \quad (72)$$

- Flow rule

$$\Psi = (\sigma_1 - \sigma_3) - (\sigma_1 + \sigma_3) \sin \psi - 2c \cos \psi \quad (73)$$

- Hardening rule (linear hardening on cohesion)

$$c = c_0 + H \epsilon_p \geq c_r \quad (74)$$

In Eq. (74), ϵ_p refers to plastic strain and H is the hardening coefficient (H negative for softening). The implementation of Mohr–Coulomb is slightly more complicated than Drucker–Prager, as it requires to check four different possibilities of return mapping: main

plane, right edge, left edge and apex. To simplify the notation, let us define

$$A = 4\mu(1 + \frac{1}{3}\sin\phi\sin\psi) + 4K\sin\phi\sin\psi, \quad (75)$$

and

$$B = 2\mu(1 + \sin\phi + \sin\psi - \frac{1}{3}\sin\phi\sin\psi) + 4K\sin\phi\sin\psi, \quad (76)$$

or

$$B = 2\mu(1 - \sin\phi - \sin\psi - \frac{1}{3}\sin\phi\sin\psi) + 4K\sin\phi\sin\psi, \quad (77)$$

depending on the case, and

$$\tilde{\varphi}(f_1, f_2) = (f_1 - f_2) - (f_1 + f_2)\sin\phi - 2c\cos\phi, \quad (78)$$

for generic variables f_1 and f_2 .

Algorithm 4 summarizes its implementation.

Appendix B. Modified Cam–Clay

The modified Cam–Clay model (MCC) is a yield criterion based on critical state Soil Mechanics. As opposed to other classical models such as Mohr–Coulomb or Drucker–Prager, the MCC set equations not only for the stress–strain relationship, but also for the overall density of the material, here represented by the specific volume $v = 1 + e = 1 + n/(1 - n)$. The two main variables related to the stress response of the material are the mean effective stress

$$p' = \frac{\sigma'_{xx} + \sigma'_{yy} + \sigma'_{zz}}{3}, \quad (79)$$

and the von Mises stress

$$q = \sqrt{\frac{1}{3}\mathbf{s} : \mathbf{s}}, \quad (80)$$

where \mathbf{s} is the deviatoric effective stress tensor

$$\mathbf{s} = \sigma' - p'\mathbf{I}. \quad (81)$$

This constitutive model is based on an associative yield criterion that depends on the pre-consolidation pressure p_c and a parameter M , which, for the triaxial compression case, is $M = 6\sin\phi/(3 - \sin\phi)$.

- Yield function and flow rule (associative flow rule)

$$\varphi = \Psi = p'^2 + p_c p' + (q/M)^2 \quad (82)$$

- Hardening rule

$$\frac{\partial p_c}{\partial \epsilon_v^p} = \frac{v}{\lambda - \kappa} p_c \quad (83)$$

λ and κ are the gradient of the normal consolidation line (NCL) and the swelling line, respectively. κ is also important to define the bulk modulus $K = (v/\kappa)p'$, which, unlike other models, is variable according to the mean effective stress p' and specific volume v . ϵ_v^p represents the volumetric plastic strain.

Given its complexity, we need to use a Newton–Raphson routine to accomplish the return mapping. The strategy is to use the Newton–Raphson algorithm to find the root of the functions

$$R_1 = \varphi, \quad (84)$$

and

$$R_2 = \Delta\epsilon_v^p + \Delta\gamma(2p' + p_c), \quad (85)$$

using $\Delta\gamma$ and $\Delta\epsilon_v^p$ as the target variables. That is, the routine stops if R_1 and R_2 become smaller than a threshold δ ($\delta = 10^{-7}$ in our simulations). Hence, we need to find the inverse of the Jacobian

$$\mathbf{J} = \begin{bmatrix} \frac{\partial R_1}{\partial \Delta\gamma} & \frac{\partial R_1}{\partial \Delta\epsilon_v^p} \\ \frac{\partial R_2}{\partial \Delta\gamma} & \frac{\partial R_2}{\partial \Delta\epsilon_v^p} \end{bmatrix} \quad (86)$$

Algorithm 4 Mohr–Coulomb return map

Input: σ'^{trial}

Output: $\sigma'^{\beta+1}$

Spectral decomposition

Trial state: $\epsilon_p^{\text{trial}} = \epsilon_p^\beta$ and $c^{\text{trial}} = c_0 + H\epsilon_p^{\text{trial}} \geq c_r$

Calculate trial yield function $\varphi^{\text{trial}} = \varphi(\sigma'^{\text{trial}})$ with Eq. (72)

if $\varphi^{\text{trial}} \leq 0$ **then**

Elastic deformation: $\sigma'^{\beta+1} = \sigma'^{\text{trial}}$

else

Plastic deformation:

(a) $\sigma'^{\beta+1}$ is on the main plane of φ

$$\Delta\gamma = \varphi^{\text{trial}}/(A + 4H\cos^2\phi)$$

$$\sigma_1^{(a)} = \sigma_1^{\text{trial}} - (2\mu(1 + \frac{1}{3}\sin\psi) + 2K\sin\psi)\Delta\gamma$$

$$\sigma_2^{(a)} = \sigma_2^{\text{trial}} + (\frac{4}{3}\mu - 2K)\sin\psi\Delta\gamma$$

$$\sigma_3^{(a)} = \sigma_3^{\text{trial}} + (2\mu(1 - \frac{1}{3}\sin\psi) - 2K\sin\psi)\Delta\gamma$$

$$\epsilon_p^{\text{trial}} = \epsilon_p^\beta + 2\cos\phi\Delta\gamma$$

Check (a): if $\sigma_1^{(a)} \geq \sigma_2^{(a)} \geq \sigma_3^{(a)}$ **then**

$$\sigma_i^{\beta+1} = \sigma_i^{(a)} \text{ and go to (d)}$$

(b) if $(1 - \sin\psi)\sigma_1^{\text{trial}} - 2\sigma_2^{\text{trial}} + (1 + \sin\psi)\sigma_2^{\text{trial}} > 0$ **then**

$\sigma'^{\beta+1}$ is on the right edge of φ (B from Eq. (76))

Solve: $\begin{cases} (A + 4H\cos^2\phi)\Delta\gamma_1 + (B + 4H\cos^2\phi)\Delta\gamma_2 = \tilde{\varphi}(\sigma_1^{\text{trial}}, \sigma_3^{\text{trial}}) \\ (B + 4H\cos^2\phi)\Delta\gamma_1 + (A + 4H\cos^2\phi)\Delta\gamma_2 = \tilde{\varphi}(\sigma_1^{\text{trial}}, \sigma_2^{\text{trial}}) \end{cases}$

$$\sigma_1^{(b)} = \sigma_1^{\text{trial}} - ((2\mu(1 + \frac{1}{3}\sin\psi) + 2K\sin\psi)(\Delta\gamma_1 + \Delta\gamma_2))$$

$$\sigma_2^{(b)} = \sigma_2^{\text{trial}} + (\frac{4}{3}\mu - 2K)\sin\psi\Delta\gamma_1 + (2\mu(1 - \frac{1}{3}\sin\psi) - 2K\sin\psi)\Delta\gamma_2$$

$$\sigma_3^{(b)} = \sigma_3^{\text{trial}} + (2\mu(1 - \frac{1}{3}\sin\psi) - 2K\sin\psi)\Delta\gamma_1 + (\frac{4}{3}\mu - 2K)\sin\psi\Delta\gamma_2$$

else

$\sigma'^{\beta+1}$ is on the left edge of φ (B from Eq. (77))

Solve: $\begin{cases} (A + 4H\cos^2\phi)\Delta\gamma_1 + (B + 4H\cos^2\phi)\Delta\gamma_2 = \tilde{\varphi}(\sigma_1^{\text{trial}}, \sigma_3^{\text{trial}}) \\ (B + 4H\cos^2\phi)\Delta\gamma_1 + (A + 4H\cos^2\phi)\Delta\gamma_2 = \tilde{\varphi}(\sigma_2^{\text{trial}}, \sigma_3^{\text{trial}}) \end{cases}$

$$\sigma_1^{(b)} = \sigma_1^{\text{trial}} - (2\mu(1 + \frac{1}{3}\sin\psi) + 2K\sin\psi)\Delta\gamma_1 + (\frac{4}{3}\mu - 2K)\sin\psi\Delta\gamma_2$$

$$\sigma_2^{(b)} = \sigma_2^{\text{trial}} + (\frac{4}{3}\mu - 2K)\sin\psi\Delta\gamma_1 - (2\mu(1 + \frac{1}{3}\sin\psi) + 2K\sin\psi)\Delta\gamma_2$$

$$\sigma_3^{(b)} = \sigma_3^{\text{trial}} + ((2\mu(1 - \frac{1}{3}\sin\psi) - 2K\sin\psi)(\Delta\gamma_1 + \Delta\gamma_2))$$

end if

$$\epsilon_p^{\text{trial}} = \epsilon_p^\beta + 2\cos\phi(\Delta\gamma_1 + \Delta\gamma_2)$$

Check (b): if $\sigma_1^{(b)} \geq \sigma_2^{(b)} \geq \sigma_3^{(b)}$ **then**

$$\sigma_i^{\beta+1} = \sigma_i^{(b)} \text{ and go to (d)}$$

(c) $\sigma'^{\beta+1}$ is on the apex of φ

$$\Delta\gamma = \sin\phi(p'^{\text{trial}} - c\cot\phi)/(\sin\phi K + H\cos\phi\cot\phi)$$

$$\sigma_1^{(c)} = \sigma_2^{(c)} = \sigma_3^{(c)} = p'^{\text{trial}} - K\Delta\gamma$$

$$\epsilon_p^{\text{trial}} = \epsilon_p^\beta + (\cos\phi/\sin\phi)\Delta\gamma$$

$$\sigma_i^{\beta+1} = \sigma_i^{(c)} \text{ and go to (d)}$$

(d) End of return map

Reassemble stress tensor (Eq. (71))

end if

Update plastic strain: $\epsilon_p^{\beta+1} = \epsilon_p^{\text{trial}}$

with the partial derivatives

$$\frac{\partial R_1}{\partial \Delta\gamma} = -\frac{12\mu}{M^2 + 6\mu\Delta\gamma} \left(\frac{q}{M} \right)^2, \quad (87)$$

$$\frac{\partial R_1}{\partial \Delta\epsilon_v^p} = 2p'K + p_cK + \frac{v}{\lambda - \kappa}p'p_c, \quad (88)$$

Algorithm 5 Modified Cam–Clay return map

Input: σ'^{trial}

Output: $\sigma'^{\beta+1}$

Retrieve p'^{trial} and q^{trial} with Eqs. (79), (80) and (81) and set $p_c^{\text{trial}} = p_c^\beta$

Calculate trial yield function $\varphi^{\text{trial}} = \varphi(\sigma'^{\text{trial}})$ with Eq. (82)

if $\varphi^{\text{trial}} \leq 0$ **then**

- Elastic deformation: $\sigma'^{\beta+1} = \sigma'^{\text{trial}}$

else

- Plastic deformation:
- (a) Preparing for the Newton–Raphson:
 - Set p_c^0, p'^0 and q^0 with their trial states
 - Set $k = 0, \Delta\gamma = 0$ and $\Delta\epsilon_v^p = 0$
- (b) Newton–Raphson:
 - do while** ($\text{error} > \delta$)
 - Calculate R_1^k, R_2^k with Eqs. (84) and (85)
 - Calculate the Jacobian J^k with Eqs. (86), (87), (88), (89)

and (90)

Solve $\begin{pmatrix} \Delta\gamma \\ \Delta\epsilon_v^p \end{pmatrix}^{k+1} = \begin{pmatrix} \Delta\gamma \\ \Delta\epsilon_v^p \end{pmatrix}^k - (J^k)^{-1} \begin{pmatrix} R_1 \\ R_2 \end{pmatrix}^k$

Update p', q and p_c :

$p'^{k+1} = p^{\text{trial}} + K\Delta\epsilon_v^p$

$q^{k+1} = \left(\frac{M^2}{M^2 + 6\mu\Delta\gamma} \right) q^{\text{trial}}$

$p_c^{k+1} = \frac{p_c^{\text{trial}}}{1 - \Delta\epsilon_v^p v / (\lambda - \kappa)}$

Calculate error: $\text{error} = \sqrt{(R_1^{k+1})^2 + (R_2^{k+1})^2}$

$k = k + 1$

end do

(c) Retrieve the effective stress tensor and pre-consolidation pressure:

$p'^{\beta+1} = p^{\text{trial}} + K\Delta\epsilon_v^p$

$s^{\beta+1} = \left(\frac{M^2}{M^2 + 6\mu\Delta\gamma} \right) s^{\text{trial}}$

$\sigma'^{\beta+1} = s^{\beta+1} + p'^{\beta+1}\mathbf{I}$

$p_c^{\beta+1} = \frac{p_c^{\text{trial}}}{1 - \Delta\epsilon_v^p v / (\lambda - \kappa)}$

(d) End of return map

end if

$$\frac{\partial R_2}{\partial \Delta\gamma} = 2p' + p_c, \quad (89)$$

$$\frac{\partial R_2}{\partial \Delta\epsilon_v^p} = 1 + \Delta\gamma \left(2K + \frac{v}{\lambda - \kappa} p_c \right). \quad (90)$$

With all parameters defined, algorithm 5 present a straight forward methodology to conduct the return mapping using the modified Cam–Clay. In algorithm 5, the letter k represents the internal iterations of the Newton–Raphson routine. Again, readers interested in understanding the details of this algorithm should refer to de Souza Neto et al. (2008), Zienkiewicz et al. (1999) or other classical authors in this subject.

References

- Asai, M., Aly, A., Sonoda, Y., Sakai, Y., 2012. A stabilized incompressible SPH method by relaxing the density invariance condition. *J. Appl. Math.* 2012, <http://dx.doi.org/10.1155/2012/139583>.
- Asai, M., Li, Y., Chandra, B., Takase, S., 2021. Fluid–rigid-body interaction simulations and validations using a coupled stabilized ISPH–DEM incorporated with the energy-tracking impulse method for multiple-body contacts. *Comput. Methods Appl. Mech. Engrg.* 377 (15), <http://dx.doi.org/10.1016/j.cma.2021.113681>.
- Bandara, S., Soga, K., 2015. Coupling of soil deformation and pore fluid flow using material point method. *Comput. Geotech.* 63, 199–214. <http://dx.doi.org/10.1016/j.compgeo.2014.09.009>.
- Barcarolo, D., Touzé, D.L., de Vuyst, F., 2014. Validation of a new fully-explicit incompressible smoothed particle hydrodynamics method. *Mech. Eng. Proc.* 1, <http://dx.doi.org/10.5151/meceng-wccm2012-16774>.
- Biot, M., 1956. Theory of propagation of elastic waves in a fluid-saturated porous solid. i. low-frequency range. *J. Acoust. Soc. Am.* 28–2, 168–178. <http://dx.doi.org/10.1121/1.1908239>.
- Blanc, T., Pastor, M., 2012. A stabilized fractional step, runge–kutta taylor SPH algorithm for coupled problems in geomechanics. *Comput. Methods Appl. Mech. Engrg.* 221–222, 41–53. <http://dx.doi.org/10.1016/j.cma.2012.02.006>.
- Bonet, J., Lok, T.-S., 1999. Variational and momentum preservation aspects of smoothed particle hydrodynamics formulations. *Comput. Methods Appl. Mech. Engrg.* 180, 97–115. [http://dx.doi.org/10.1016/S0045-7825\(99\)00051-1](http://dx.doi.org/10.1016/S0045-7825(99)00051-1).
- Bromhead, E., Cooper, M., Petley, D., 1998. The selborne cutting slope stability experiment (CD-ROM). *Selborne Data Collect. CD*.
- Bui, H., Bguyen, G., 2021. Smoothed particle hydrodynamics (SPH) and its applications in geomechanics: from solid fracture to granular behaviour and multiphase flows in porous media. *Comput. Geotech.* 138, 104315. <http://dx.doi.org/10.1016/j.comgeo.2021.104315>.
- Bui, H., Fukagawa, R., 2009. A first attempt to solve soil–water coupled problem by SPH. *Jpn. Terramech.* 29, 33–38.
- Bui, H., Fukagawa, R., 2013. An improved SPH method for saturated soils and its application to investigate the mechanisms of embankment failure: Case of hydrostatic pore-water pressure. *Int. J. Numer. Anal. Methods Geomech.* 37, 31–50. <http://dx.doi.org/10.1002/nag.1084>.
- Bui, H., Fukagawa, R., Sako, K., Ohno, S., 2008. Lagrangian meshfree particles method (SPH) for large deformation and failure flows of geomaterial using elastic–plastic soil constitutive model. *Int. J. Numer. Anal. Methods Geomech.* 32, 1537–1570. <http://dx.doi.org/10.1002/nag.688>.
- Bui, H., Nguyen, G., 2017. A coupled fluid–solid SPH approach to modelling flow through deformable porous media. *Int. J. Solids Struct.* 125, 244–264. <http://dx.doi.org/10.1016/j.ijsolstr.2017.06.022>.
- Cascini, L., Cuomo, S., Pastor, M., Sorbini, G., Piciullo, L., 2014. SPH Run-out modelling of channelised landslides of the flow type. *Geomorphology* 214, 502–513. <http://dx.doi.org/10.1016/j.geomorph.2014.02.031>.
- Cooper, M., Bromhead, E., Petley, D., Grant, D., 1998. The selborne cutting stability experiment. *Geotechnique* 48, 83–101. <http://dx.doi.org/10.1680/geot.1998.48.1.83>.
- Cummins, S., Rudman, M., 1999. An SPH projection method. *J. Comput. Phys.* 152, 584–607. <http://dx.doi.org/10.1006/jcph.1999.6246>.
- Faheti, R., Manzari, M., 2011. Error estimation in smoothed particle hydrodynamics and a new scheme for second derivatives. *Comput. Math. Appl.* 61 (2), 482–498. <http://dx.doi.org/10.1016/j.camwa.2010.11.028>.
- Ganzenmüller, G., 2015. An hourglass control algorithm for Lagrangian smooth particle hydrodynamics. *Comput. Methods Appl. Mech. Engrg.* 286, 87–106. <http://dx.doi.org/10.1016/j.cma.2014.12.005>.
- Gingold, R., Monaghan, J., 1977. Smoothed particle hydrodynamics: theory and application to non-spherical stars. *Astron. Soc.* 181, 375–389. <http://dx.doi.org/10.1093/mnras/181.3.375>.
- Khayyer, A., Gotoh, H., Shao, S., 2008. Corrected incompressible SPH method for accurate water-surface tracking in breaking waves. *Coast. Eng.* 55 (3), 236–250. <http://dx.doi.org/10.1016/j.coastaleng.2007.10.001>.
- Koshizuka, S., Oka, Y., 1996. Moving-particle semi-implicit method for fragmentation of incompressible fluid. *Nucl. Sci. Eng.* 123, 421–434. <http://dx.doi.org/10.13182/NSE96-A24205>.
- Kularathna, S., Liang, W., Zhao, T., Chandra, B., Zhao, J., Soga, K., 2021. A semi-implicit material point method based on fractional-stepmethod for saturated soil. *Int. J. Numer. Anal. Methods Geomech.* <http://dx.doi.org/10.1002/nag.3207>.
- Lee, C.H., Gil, A.J., Gredo, G., Kulasegaram, S., Bonet, J., 2016. A new jemeson-Schmidt-Turkel smooth particle hydrodynamics algorithm for large strain explicit fast dynamics. *Comput. Methods Appl. Mech. Engrg.* 311, 71–111. <http://dx.doi.org/10.1016/j.cma.2016.07.033>.
- Lian, Y., Bui, H., Bguyen, G., Tran, H., Haque, A., 2021. A general SPH framework for transient seepage flows through unsaturated porous media considering anisotropic diffusion. *Comput. Method Appl. Mech. Engrg.* 387, 114169. <http://dx.doi.org/10.1016/j.cma.2021.114169>.
- Lin, C., Pastor, M., Li, T., Liu, X., Lin, C., Qi, H., Sheng, T., 2019. A PFE/IE – SPH joint approach to model landslides from initiation to propagation. *Comput. Geotech.* 114, 103153. <http://dx.doi.org/10.1016/j.compgeo.2019.103153>.
- Lucy, L., 1977. A numerical approach to the testing of the fusion process. *Astron. J.* 82, 1013–1024. <http://dx.doi.org/10.1086/112164>.
- Maeda, K., Sakai, H., Sakai, M., 2004. Development of seepage failure analysis method of ground with smoothed particle hydrodynamics (in Japanese). *J. Appl. Mech.* 7, 775–786.
- Maeda, K., Sakai, H., Sakai, M., 2006. Development of seepage failure analysis method of ground with smoothed particle hydrodynamics. *Struct. Eng./Earthq. Eng.* 23 (2), 307–319. <http://dx.doi.org/10.2208/jscseee.23.307s>.
- Monaghan, J., 1992. Smoothed particle hydrodynamics. *Annu. Rev. Astron. Astrophys.* 30, 543–574. <http://dx.doi.org/10.1146/annurev.aa.30.090192.002551>.
- Morikawa, D., Asai, M., 2021. Coupling total lagrangian SPH-EISPH for fluid-structure interaction with large deformed hyperelastic solid bodies. *Comput. Methods Appl. Mech. Engrg.* 381, <http://dx.doi.org/10.1016/j.cma.2021.113832>.

- Morikawa, D., Asai, M., Idris, N., Imoto, Y., Isshiki, M., 2019. Improvements in highly viscous fluid simulation using a fully implicit SPH method. *Comput. Part. Mech.* 6, 529–544. <http://dx.doi.org/10.1007/s40571-019-00231-6>.
- Morikawa, D., Senadheera, H., Asai, M., 2021. Explicit incompressible smoothed particle hydrodynamics in a multi-gpu environment for large-scale simulations. *Comput. Part. Mech.* 8, 493–510. <http://dx.doi.org/10.1007/s40571-020-00347-0>.
- Morris, J., Fox, P., Zhu, Y., 1997. Modeling low Reynolds number incompressible flows using SPH. *J. Comput. Phys.* 136 (1), 214–226. <http://dx.doi.org/10.1006/jcph.1997.5776>.
- Naili, M., Matsushima, T., Yamada, Y., 2005. A 2D smoothed particle hydrodynamics method for liquefaction induced lateral spreading analysis. *J. Appl. Mech.* 8, 591–599. <http://dx.doi.org/10.2208/journalam.8.591>.
- Pastor, M., Blanc, T., Drempetic, V., Dutto, P., Stickle, M.M., Yague, A., 2015. Modelling of landslides: and SPH approach. *CMES* 109–110 (2), 183–220. <http://dx.doi.org/10.3970/cmes.2015.109.183>.
- Pereira, G., Cleary, P., Lemiale, V., 2017. SPH Method applied to compression of solid materials for a variety of loading conditions. *Appl. Math.* 44, 72–90. <http://dx.doi.org/10.1016/j.apm.2016.12.009>.
- Pozorski, J., Wawrenzuk, A., 2002. SPH Computation of incompressible viscous flows. *J. Theoret. Appl. Mech.* 40, 917–937.
- Randles, P., Libersky, L., 1996. Smoothed particle hydrodynamics: some recent improvements and applications. *Comput. Methods Appl. Mech. Engrg.* 139, 375–408. [http://dx.doi.org/10.1016/S0045-7825\(96\)01090-0](http://dx.doi.org/10.1016/S0045-7825(96)01090-0).
- Schoenberg, I.J., 1964. Spline interpolation and best quadrature formulae. *Bull. Amer. Math. Soc.* 70 (1), 143–148. <http://dx.doi.org/10.1090/S0002-9904-1964-11054-5>.
- de Souza Neto, E., Perić, D., Owen, D., 2008. Computational Methods for Plasticity: Theory and Applications. John Wiley & Sons, Ltd, <http://dx.doi.org/10.1002/9780470694626>.
- Zhao, S., Bui, H., Lemiale, V., Nguyen, G., Darve, F., 2019. A generic approach to modelling flexible confined boundary conditions in SPH and its application. *Int. J. Numer. Anal. Methods Geomech.* 43, 1005–1031. <http://dx.doi.org/10.1002/nag.2918>.
- Zienkiewicz, O., Chan, A., Pastor, M., Schrefler, B., Shiomi, T., 1999. Computational Geomechanics with Special Reference to Earthquake Engineering. John Wiley & Sons, Ltd.